Innovative β-ketoenamine-linked covalent organic frameworks: Tailored D1-A-D2-A structure for highly efficient photocatalytic degradation of organic pollutants

Yun-Zhen Xiao [a], Ahmed A.K. Mohammed [b], Shiao-Wei Kuo [a], Ahmed F.M. EL-Mahdy [a,b,*]

[a] *Department of Materials and Optoelectronic Science, National Sun Yat-Sen University, Kaohsiung 80424, Taiwan*
[b] *Chemistry Department, Faculty of Science, Assiut University, Assiut 71516, Egypt*

ARTICLE INFO

ABSTRACT

Covalent organic frameworks (COFs) are prospective photocatalysts for the treatment of organic pollutants; however, their photocatalytic efficacy is restricted by their quick charge recombination and non-optimal energy band configuration. Herein, we report the synthesis of two donor–acceptor β-ketoenamine-linked COFs with a D1-A-D2-A structure (AZO-TFP-BT-TFP and AZO-TFP-MBT-TFP COFs) for high-performance photocatalytic degradation of cationic and anionic organic dyes. This remarkable performance originates from their high surface area, excellent crystallinity, high separation of photogenerated electron/hole pairs, large-scale electron delocalization, effective charge transfer, and favorable band gap configuration. The photocatalytic degradation of organic pollutants, specifically the cationic organic dye Rhodamine B and the anionic organic dye methyl orange, was achieved with a significant degree of efficacy using both COFs. In particular, Rhodamine B can be completely photodegraded by AZO-TFP-BT-TFP COF under visible light irradiation within 3 h, with a degraded efficiency of 97.70 ± 0.51 % and a reaction rate constant of 1.21 h^{-1}. The mechanism investigation presents strong evidence that the effective photodegradation by AZO-TFP-BT-TFP COF is chemically explained by the presence of holes, hydroxyl radicals, and superoxide radicals. Our work, the first systematic study of incorporating the D1-A-D2-A structure in COFs, offered a design method for the strong degradation of organic contaminants employing stable photocatalysts.

1. Introduction

Covalent Organic Frameworks (COFs) are porous polymers with a well-defined crystal structure, formed through strong covalent bonds between light elements such as H, B, C, N, and O [1]. Moreover, owing to the exceptional chemical stability of COFs in organic solvents [2], they can endure harsh conditions of acidity and alkalinity [3]. Additionally, they exhibit permanent porosity [4], high surface areas [5], and orderly arranged pores [6], among other merits. Presently, COFs have been used in many applications such as adsorption [7], separation [8], H₂ evolution [9], energy storage [10], sensor [11], anion conduction [12], drug delivery [13], proton and ion transport [14]. Furthermore, a notable advantage of COFs over other porous materials is their predictable crystal structures [12]. Each monomer possesses distinct geometric characteristics, enabling the anticipation of the synthesized COFs' structures through topology diagrams [3], yielding highly ordered

geometrical arrangements [4]. Studies indicate that through molecular design, COFs can precisely regulate their photoelectric properties, thereby enhancing photocatalytic activity through structural modifications [15,16]. COFs exhibit prominent optical absorbance and facilitate charge mobility over the whole polymeric structure, both of which are essential for the process of photocatalysis [17,18]. The arranged porosity of COF facilitates the rapid transport of hydrogen, carbon dioxide, and degradable substances to the catalytic site, hence enhancing catalytic activity [19,20]. Unfortunately, the use of COFs as photocatalysts is hindered by the presence of high exciton binding energies and low charge carrier mobilities, resulting in subpar photocatalytic activity [21–23]. However, these issues are mitigated when donor–acceptor (D-A) structured COFs are constructed. The development of a D-A-based COF would be very advantageous due to its ability to demonstrate intramolecular charge transfer processes resulting from the absorption of visible light, making it suited for metal-free

---
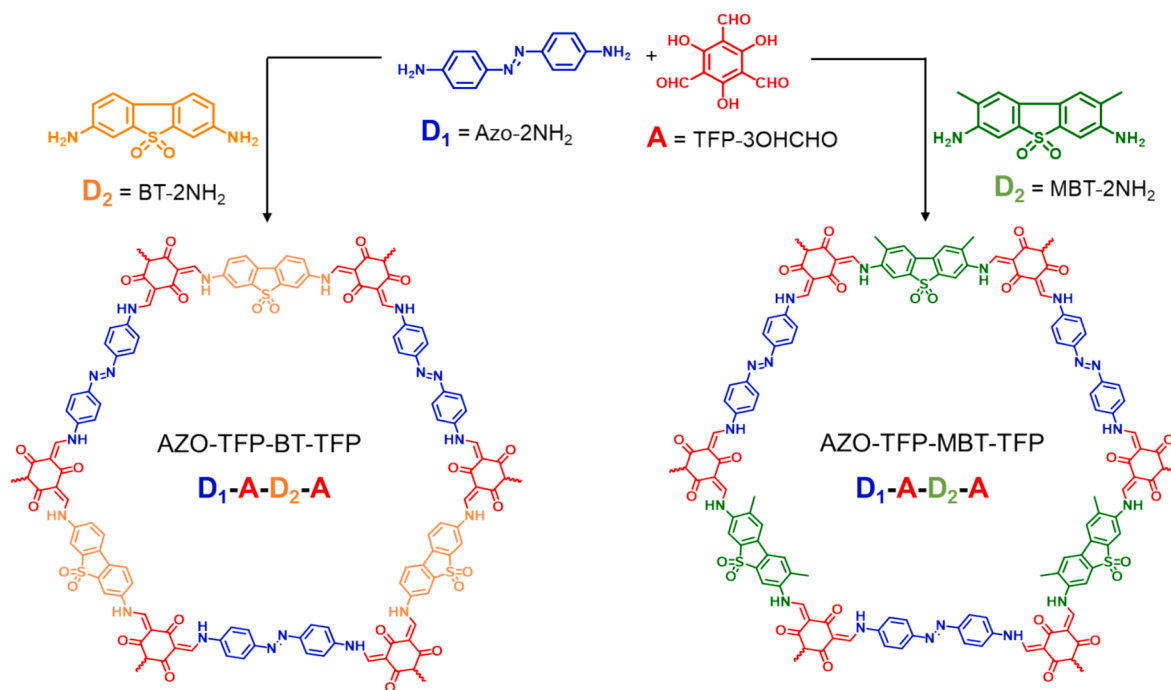
Scheme 1. Synthesis of the donor–acceptor COFs with a D1-A-D2-A structure.

photocatalysis [23–25]. In addition, the incorporation of a donor–acceptor moiety in a polymer network enhances the process of separating charges by reducing the strength of the exciton binding, resulting in highly efficient catalysis [23–25]. Several COFs have been investigated for their capacity to photocatalytic degradation of organic pollutants [26–31]. Therefore, the task of developing donor and acceptor COFs that are safe for the environment as semiconductors for the photocatalytic degradation of natural dyes in water is still a challenging endeavor.

Industrialization and human activities led to severe water pollution [32–34]. This indirectly impacts human health and inflicts significant harm on the environment [35,36]. Consequently, over the past decade, an increasing number of researchers have started to pay attention to the issue of water pollution [37,38]. Research findings underscore that wastewater produced from industrial processes frequently contains hazardous chemicals that pose substantial environmental risks. Notably, these chemicals often resist effective removal through biodegradation processes [39]. In this experimental study, methyl orange (MO) and rhodamine B (RhB) are prevalent components in a range of everyday objects, including paints [40], ballpoint pens, fireworks, stamp ink [41], textiles [42], pharmaceuticals [43], paper [44], and various other products commonly encountered in daily life. Furthermore, both of these organic pollutants can exert adverse effects on human health [45]. Research findings suggest that MO has the potential to cause damage to the eyes and the central nervous system. Similarly, RhB has been associated with inducing gastrointestinal irritation, eye and respiratory infections, skin allergies, and various other symptoms [46,47]. To enhance water quality, numerous advanced technologies have been devised for the removal of organic dyes from wastewater. These encompass biological treatment [48,49], dye adsorption [50], photocatalysis [51], ion exchange removal [52,53], and other innovative methods [54]. Among these techniques, dye adsorption stands out as the most commonly employed approach. This preference is attributed to its ease of operation, high removal efficiency, and cost-effectiveness [55–59]. Nevertheless, adsorption methods present a significant drawback as they solely adsorb pollutants without degrading them, giving rise to the issue of secondary pollution [39,60,61]. To counter this concern, photocatalysis technology emerged as a promising solution. This innovative approach addresses the limitation of adsorption by facilitating the degradation of pollutants under sunlight and at room temperature, thereby fundamentally resolving the challenge of secondary pollution associated with traditional adsorption methods [62,63]. In comparison to other technologies, photocatalytic degradation offers distinct advantages in achieving what is commonly referred to as "green" environmental remediation [64]. Consequently, in recent years, a segment of researchers has initiated studies on the application of porous polymers in the photodegradation of dyes [65–68].

The selection of covalent bonds and photoactive precursors is crucial in the development of efficient two-dimensional (2D) COF photocatalysts. Hence, we are interested in exploring novel 2D COFs that exhibit D1-A-D2-A type structures and extended conjugation frameworks to boost the photocatalytic activity. The compound 1,3,5-triformylphloroglucinol (TFP-3OHCHO) can form a resonance configuration called enol-imine when it combines with arylamine. The isomerization process of TFP-3OHCHO leads to the synthesis of carbonyl, culminating in the [6] radialene structure, which is a skeleton with a shortage of electrons [69]. Furthermore, the conversion of enol-imine to the β-keto-enamine resonance structure of the TFP-3OHCHO component significantly enhances both the chemical stability and photoelectric characteristics by facilitating hydrogen-bond formation. The compounds 4′4-Diaminoazobenzene (Azo-2NH$_2$) and 3,7-diaminodibenzo[b,d]thiophene-5,5-dioxide derivatives (BT-2NH$_2$ and MBT-2NH$_2$) are electron donors due to the presence of electron-rich arylamines in their structure. The Azo unit is an effective electron donor with an extended π-conjugated structure, and it has desirable characteristics of charge transport and electron donation [70]. The BT unit has both a planar structure, which enhances stability, and a lengthy π-conjugated structure. These features enable the photogenerated separation and movement of charge carriers, resulting in excellent photoelectric activity [71]. To the best of our knowledge, there have not been any prior studies on synthesizing 2D COFs based on β-keto-enamine D1-A-D2-A type structure. The current study focuses on synthesizing two donor–acceptor β-ketoenamine-linked covalent organic frameworks with a D1-A-D2-A structure. These COFs, named AZO-TFP-BT-TFP and AZO-TFP-MBT-TFP COFs, were synthesized through the one-pot three-component condensation of TFP-3OHCHO acceptor with Azo-2NH$_2$ and 3,7-diaminodibenzo[b,d]
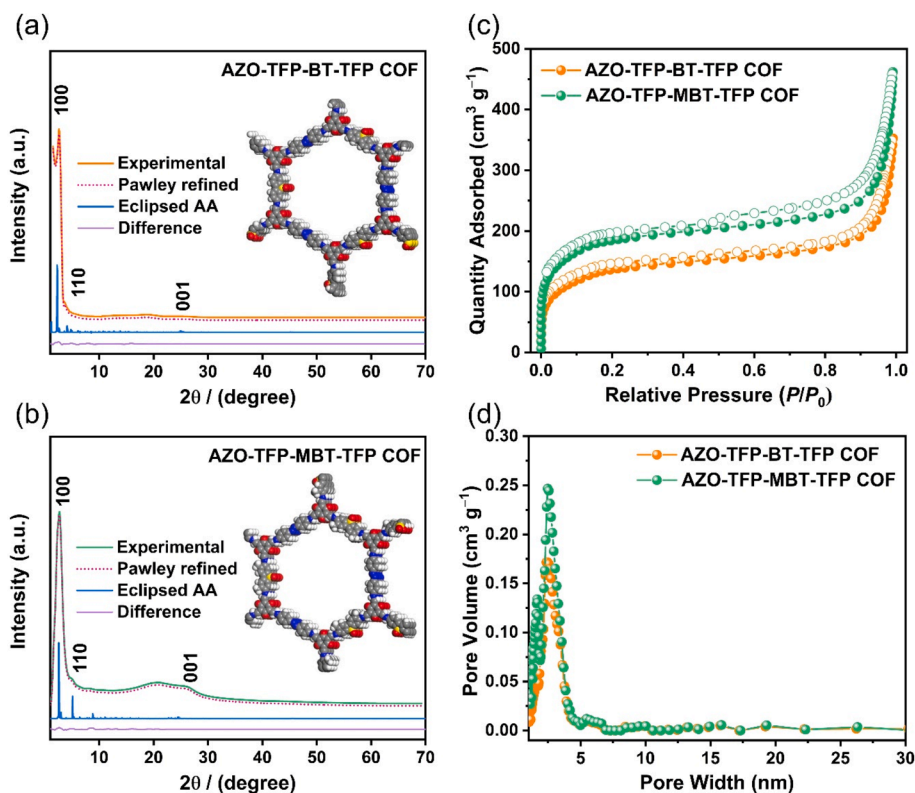
Fig. 1. PXRD patterns of (a) AZO-TFP-BT-TFP and (b) AZO-TFP-MBT-TFP COFs. (c) Nitrogen sorption isotherms at 77 K and (d) pore size distributions of AZO-TFP-BT-TFP and (b) AZO-TFP-MBT-TFP COFs.

thiophene-5,5-dioxide (BT-2NH$_2$) donors, and of TFP-3OHCHO acceptor with Azo-2NH$_2$ and 3,7-diamino-2,8-dimethyldibenzo[b,d]thiophene 5,5-dioxide (MBT-2NH$_2$) donors (Scheme 1). The employment of resulting COFs for the process of photocatalytic degradation of organic chemical dyes was investigated.

2. Experimental section

2.1. Materials

Chemical reagents and solvents used in the synthesis process were obtained from commercial sources and used as received. 4′4-dia-minoazobenzene and mesitylene were purchased from Alfa Aesar. 1,4-dioxane, acetic acid, hexane, and tetrahydrofuran were obtained from Honeywell Fluka.

2.2. Preparation of AZO-TFP-BT-TFP and AZO-TFP-MBT-TFP COFs

In a Schlenk storage tube, BT-2NH$_2$ (87.9 mg, 0.356 mmol) or MBT-2NH$_2$ (97.92 mg, 0.356 mmol), Azo-2NH$_2$ (75.76 mg, 0.356 mmol), and TFP-3OHCHO (100 mg, 0.475 mmol) were dissolved in 1,4-dioxane (4 ml). After thorough mixing, mesitylene (4 ml) and 6 M AcOH (0.8 ml) were sequentially added. The solution underwent ultrasonic agitation to ensure homogeneous solvent mixing. The Schlenk storage tube was then immersed in a liquid nitrogen bath for solidification, followed by vacuum evacuation for 10 min. Subsequently, the tube was transferred to a water bath, and the solvent was liquefied by rinsing the bottle with water using a dropper. The process was repeated multiple times. After 3 days in an oil bath at 120 °C, the Schlenk storage tube cooled down to room temperature. The precipitate is filtered out and washed twice with Methanol, THF, and Hexane. Light-red powders for AZO-TFP-BT-TFP and AZO-TFP-MBT-TFP COFs were obtained by vacuum drying the solid at 80 °C overnight.

3. Results and discussion

3.1. Synthesis and characterization of COFs

Scheme 1 illustrates our synthesis of two donor–acceptor β-ketoen-amine-linked COFs with a D1-A-D2-A structure using the precursor materials. The desired AZO-TFP-BT-TFP COF was synthesized by combining TFP-3OHCHO (Scheme S1 and Figures S1–S3), Azo-2NH$_2$, and BT-2NH$_2$ (Scheme S2 and Figures S4–S6) in a one-pot three-component condensation reaction, with a molar ratio of 2:1.5:1.5. Similarly, the AZO-TFP-MBT-TFP COF was obtained by reacting TFP-3OHCHO, Azo-2NH$_2$, and MBT-2NH$_2$ (Scheme S3 and Figures S7–S9) in a one-pot three-component condensation reaction, with a molar ratio of 2:1.5:1.5. Both COFs were synthesized in a three-day process using an acidic catalyst of 6 M CH$_3$COOH and a combination of 1,4-dioxane and mesitylene in a ratio of 1:1 (Scheme S4 and S5). The chemical constituents of the COFs were verified using FTIR, solid-state ^{13}C cross-polarization magic-angle-spinning (CP MAS) NMR spectroscopy, and X-ray photoelectron spectroscopy (XPS). The FTIR spectra of AZO-TFP-BT-TFP and AZO-TFP-MBT-TFP COFs exhibited characteristics peaks at 3392–3380 and 1580–1578 cm^{-1}, which could be attributed to the N–H and N═N chemical bonds, respectively, as well as C═O bonds at 1621–1620 cm^{-1}. The peaks seen at 1290–1147 and 843–842 cm^{-1} were identified as resulting from the presence of S═O and C–S bonds, respectively (Figures S10 and S11). The CH$_3$ bonds in the AZO-TFP-MBT-TFP COF were responsible for the subsequent observation of a peak at 1410 cm^{-1} (Figure S11). The solid-state ^{13}C NMR spectra of the AZO-TFP-BT-TFP and AZO-TFP-MBT-TFP COFs exhibited peaks at 185.63 and 185.27 ppm, respectively, corresponding to their carbonyl (C═O) groups (Figures S12 and S13). In addition, the ^{13}C NMR spectrum of AZO-TFP-MBT-TFP COF featured a peak at 18.01 ppm, representing the CH$_3$ groups (Figure S13). The COF catalysts were analyzed using X-ray photoelectron spectroscopy (XPS) to determine the compositions and orbital distributions of the S, C, N, and O elements.

Figure S14 displays five separate peaks at energy levels of 168, 231, 284, and 399 eV, which correspond to the presence of sulfur (2p), sulfur (1s), carbon, and nitrogen atoms in the structures. Additionally, there is a peak at 530 eV, indicating the presence of adsorbed water and oxygen. Calculating the donor and acceptor element atomic percentages yielded the theoretical element ratio. After sensitivity factor adjustment, the experimental element ratio was computed from each species' peak area in the XPS survey of COFs. The two ratios are shown in Tables S1 and S2, demonstrating a strong correlation.

We conducted an XPS curve fitting analysis on the S 2p, C 1s, N 1s, and O 1s orbitals to get more insights into the various S, C, N, and O species found in the COFs. The S 2p orbital of the AZO-TFP-BT-TFP COF exhibited two distinct peaks at 167.02 and 168.24 eV, corresponding to the S $2p_{1/2}$ and S $2p_{3/2}$ spin orbits respectively, with a ratio of 2:1 (Figure S15, Table S3). Similarly, the AZO-TFP-MBT-TFP COF had the same two spin orbits at 167.32 and 168.51 eV. Figure S15 and Table S3 demonstrate that the AZO-TFP-BT-TFP COF exhibited four main peaks in the C 1s spectra. These peaks corresponded to C=C, C–S, C–N, and C=O, with respective energy values of 283.74, 284.27, 284.98, and 285.83 eV, respectively. Further, the C 1s orbital of the AZO-TFP-BT-TFP COF was separated into four peaks, positioned at 283.90 eV for the C=C bond, at 284.61 eV for the C–S bond, at 285.31 eV for the C–N bond, and 286.16 eV for the C=O bond. The N 1s orbital of the AZO-TFP-BT-TFP COF exhibited two distinct peaks at 398.87 and 400.98 eV, corresponding to the C–N and N=N bonds, respectively (Figure S15 and Table S3). The AZO-TFP-MBT-TFP COF also displayed these two bonds at 399.11 and 401.01 eV. Furthermore, the AZO-TFP-BT-TFP COF displayed three distinct peaks in the O 1s spectra: S=O=S, C=O, and H_2O at energy values of 529.68, 530.98, and 532.56 eV, respectively. On the other hand, the AZO-TFP-MBT-TFP COF demonstrated similar peaks at energy values of 529.74, 531.14, and 532.90 eV, respectively (Figure S15 and Table S3). The fitting ratio of the S, C, N, and O species was summarized in Table S4. The findings have verified the interplay between TFP-3OHCHO, Azo-2NH₂, and BT-2NH₂ monomers, leading to the formation of the AZO-TFP-BT-TFP COF framework. Similarly, the interaction of TFP-3OHCHO, Azo-2NH₂, and MBT-2NH₂ has resulted in the formation of the AZO-TFP-MBT-TFP COF framework. Furthermore, the assembly of AZO-TFP-BT-TFP and AZO-TFP-MBT-TFP COFs was validated using elemental analysis. The experimental data for the AZO-TFP-BT-TFP and AZO-TFP-MBT-TFP COFs showed C contents of 66.02 % and 66.14 %, respectively; nitrogen N contents of 10.15 % and 10.28 %, respectively; S contents of 4.27 % and 4.23 %, respectively; and H contents of 3.22 % and 3.31 %, respectively (Table S5). These values were found to be in good agreement with the theoretical values.

3.2. Crystallinity, thermal stability, porosity, and morphology

The powder X-ray diffraction (PXRD) technique was used to examine the crystal structures of AZO-TFP-BT-TFP and AZO-TFP-MBT-TFP COFs, as shown in Fig. 1a and 1b. The PXRD pattern of AZO-TFP-BT-TFP (Fig. 1a) exhibited a prominent peak at 2.59°, which we ascribe to the reflection of the (1 0 0) plane. Additionally, there were relatively weaker reflections from the (1 1 0) plane at 3.81°. The partially wide peak observed at 25.17° was identified as the result of the reflection of the (0 0 1) plane caused by the π-stacking interaction between the layers of the COF. The AZO-TFP-MBT-TFP COF displays a prominent peak at 2.62° and smaller peaks at 5.15° and 24.73°, which correspond to the reflection of the (1 0 0), (1 1 0), and (0 0 1) planes, respectively (Fig. 1b). The d_{100} and interlayer distance for AZO-TFP-BT-TFP COF were determined to be 3.40 nm and 3.53 Å, respectively, using the Bragg equation. For AZO-TFP-MBT-TFP COF, these values were 3.36 nm and 3.59 Å. These results indicated that the presence of a methyl group in the pore skeleton leads to a reduction in d_{100}. Subsequently, Material Studio was used to model the frameworks of AZO-TFP-BT-TFP and AZO-TFP-MBT-TFP COFs. Results showed that both COFs should have triclinic topologies. Pawley XRD refinements of the AZO-TFP-BT-TFP and AZO-TFP-

MBT-TFP COFs (Fig. 1a and 1b, purple curves) showed few inconsistencies with experimental PXRD patterns (Fig. 1a and 1b, orange and green curves) indicated their consistency (Fig. 1a and 1b, violet curves). We conducted simulations of the AA-eclipsed stacking structures of the AZO-TFP-BT-TFP and AZO-TFP-MBT-TFP COFs to get further data on their unit cell properties. The simulated XRD patterns (Fig. 1a and 1b, blue curves) exhibited a high degree of agreement with the experimental patterns. The refinement results showed that the unit cell parameters for AZO-TFP-BT-TFP COF were very close to the predicted values, with good agreement factors (a = 70.5632 Å, b = 70.5632 Å, c = 4.1234 Å, α = 90.00°, β = 90.00°, γ = 120.00°). Similarly, for AZO-TFP-MBT-TFP COF, the unit cell parameters were also close to the predicted values (a = 70.5345 Å, b = 70.5345 Å, c = 4.1134 Å, α = 90.00°, β = 90.00°, γ = 120.00°). The specific values can be found in Tables S6 and S7.

Thermogravimetric analysis (TGA) was used to assess the thermal stability of AZO-TFP-BT-TFP and AZO-TFP-MBT-TFP COFs. The results showed that these COFs had excellent thermal stability, with decomposition temperatures (T_{d10}) of 446 °C and 469 °C and a char yield of 53 % and 55 %, respectively (Figure S16, Table S8). The exceptional thermal stability of these COFs may be ascribed to their significant level of condensation.

Considering the significance of pore size and surface area in photocatalytic materials to evaluate the porosity features of the COFs, we conducted N_2 sorption isothermal tests at 77 K. The AZO-TFP-BT-TFP and AZO-TFP-MBT-TFP COFs displayed type IVb isotherms, which indicate that our COFs have a mesoporous structure (Fig. 1c). The AZO-TFP-BT-TFP and AZO-TFP-MBT-TFP COFs were found to have specific surface areas of 503 and 681 $m^2 \, g^{-1}$, respectively, as calculated by the Brunauer-Emmett-Teller (BET) method. The reduced surface area of AZO-TFP-BT-TFP could be attributed to its lower crystallinity, which is a consequence of the decreased solubility of the BT-2NH₂ precursor in organic solvents. The pore widths obtained for AZO-TFP-BT-TFP and AZO-TFP-MBT-TFP COFs by applying nonlocal density functional theory (DFT) models to the N_2 isotherms were 2.45 and 2.49 nm, respectively (Fig. 1d). We examined the geometry and internal architectures of these COFs using transmission electron microscopy (TEM) and field-emission scanning electron microscopy (FE-SEM). The TEM images of AZO-TFP-BT-TFP and AZO-TFP-MBT-TFP COFs revealed that both COFs exhibited self-assembly behavior, forming thin, non-spherical, and curved fibers (Figure S17). These fibers had a length of several micrometers and a width of around 30–40 nm. The FE-SEM images of AZO-TFP-BT-TFP and AZO-TFP-MBT-TFP COFs verified the presence of a curved fiber structure (Figures S18 and S19). Furthermore, the elemental mapping conducted using energy-dispersive X-ray spectroscopy (EDS) demonstrated that carbon, nitrogen, oxygen, and sulfur atoms are uniformly distributed throughout the framework of both AZO-TFP-BT-TFP and AZO-TFP-MBT-TFP COFs (Figures S18 and S19). The chemical stability of the AZO-TFP-BT-TFP and AZO-TFP-MBT-TFP COFs in water was assessed by immersing 20 mg of each COF in water for a duration of 4 days, followed by separation using vacuum filtering. Figure S20 demonstrates that the FTIR signals remained unchanged with no substantial alteration following immersion in water, suggesting the remarkable chemical stability of AZO-TFP-BT-TFP and AZO-TFP-MBT-TFP COFs in aqueous environments.

3.3. Photophysical and electrochemical properties

For photocatalysts to have effective photocatalytic performance, they must possess suitable optical gaps, as well as desirable photophysical and electrochemical characteristics. Therefore, ultraviolet–visible diffuse reflectance spectroscopy (UV–Vis DRS), photocurrent measurement, and electrochemical impedance spectroscopy (EIS) were used to examine these characteristics of AZO-TFP-BT-TFP and AZO-TFP-MBT-TFP COFs in solid-state form. Figures S21 and S22 demonstrate that both COFs have wide light absorption ranges that
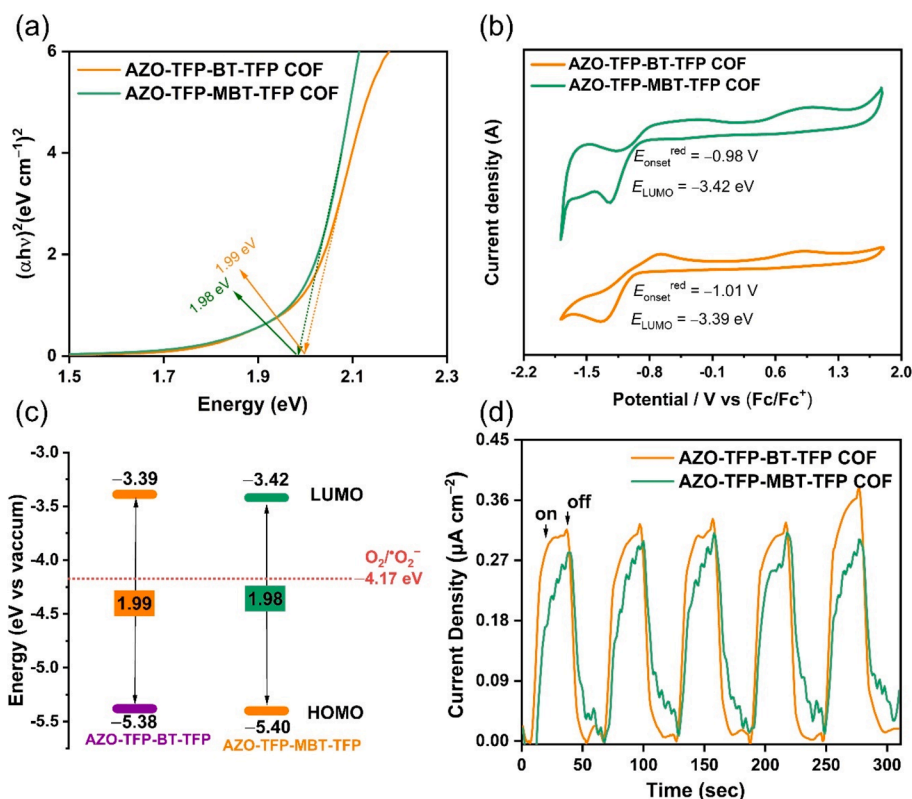
Fig. 2. (a) Tauc plots from the UV–Vis spectra, (b) cyclic voltammograms, (c) energy level diagrams, and (d) periodic on/off photocurrent responses of AZO-TFP-BT-TFP and (b) AZO-TFP-MBT-TFP COFs.

extend up to 800 nm. The maximum absorption intensities were observed at wavelengths of 566 nm for AZO-TFP-BT-TFP COF and 569 nm for AZO-TFP-MBT-TFP COF, indicating their excellent capacity to capture visible light. The slight red-shifting of the absorption signal of AZO-TFP-MBT-TFP COF in comparison to AZO-TFP-BT-TFP COF can be attributed to the presence of methyl groups, which enhanced the donor ability of MBT units. The optical bandgap of these COFs was determined using Tauc plots and found to be 1.99 and 1.98 eV, respectively (Fig. 2a). Afterward, cyclic voltammetry (CV) was used to determine the levels of the lowest unoccupied molecular orbitals (LUMOs) for these COFs. Subtracting the band gaps from the LUMO energy levels yielded the highest occupied molecular orbital (HOMO) levels (Fig. 2b and 2c). The energy levels of the HOMO and LUMO were −5.38 and −3.39 eV, respectively, for AZO-TFP-BT-TFP COF and were −5.40 and −3.42 eV, respectively, for AZO-TFP-MBT-TFP COF (Fig. 2c and Table S9). The greater negative value of the LUMO position for the AZO-TFP-MBT-TFP COF compared to the AZO-TFP-BT-TFP COF might be ascribed to the existence of methyl groups [72]. The initial stage in optical photocatalytic reactions involves the generation and movement of electron-hole pairs produced by light. Thus, the photocurrent and EIS measurements were used to evaluate the efficiency of the charge generation and transfer process. We used a conventional three-electrode apparatus to quantify the photocurrent and EIS measurement of our synthesized COFs. Both AZO-TFP-BT-TFP and AZO-TFP-MBT-TFP COFs displayed significant photocurrent density during intermittent irradiation with visible light (Fig. 2d), suggesting their effective transfer of the generated electric charge. Furthermore, the Nyquist plots verified that both AZO-TFP-BT-TFP and AZO-TFP-MBT-TFP COFs exhibited excellent electrical conductivity and little resistance to charge transfer (Figure S23). The photoluminescence (PL) spectrum was used to evaluate the efficiency of charge carrier separation and trapping. The reduction in PL emission seen in AZO-TFP-BT-TFP COF could be attributed to a higher chance of nonradiative separation of charge carriers. Conversely, the

higher emission in AZO-TFP-MBT-TFP COF suggested a more favorable mechanism for radiative recombination of electron-hole pairs (Figure S24) [73]. The reduced emission in AZO-TFP-BT-TFP COF suggested that a higher number of photoexcited electrons are likely involved in the photocatalytic activity instead of experiencing recombination with holes via fluorescent emission. In addition, these concepts were strengthened by examining the fluorescence lifetime decays of the AZO-TFP-BT-TFP and AZO-TFP-MBT-TFP COFs (Figure S25). The fluorescence lifetime of the AZO-TFP-BT-TFP COF was 3.48 ns, whereas the fluorescence lifetime of the AZO-TFP-MBT-TFP was 2.51 ns. This suggests that the AZO-TFP-BT-TFP COF has a higher efficiency in separating charge carriers. The combined findings validate that our COFs have a notable ability to transfer photogenerated electrons under effective illumination.

To verify the presence of the D1-A-D2-A structure in β-ketoenamine-linked COFs, we conducted DFT calculations at the B3LYP level using the 6–31 G (d,p) basis set to study the structure–property interactions of the AZO-TFP, BT-TFP, and MBT-TFP pairings. Fig. 3a-c show that the AZO, BT, and MBT units functioned as electron donors, whereas the TFP unit served as an electron acceptor. While the electron concentrations of the LUMO states in the three pairings were mostly concentrated on the TFP fragment, the HOMO states were dispersed over the TFP unit as well as the AZO, BT, and MBT fragments. The findings verified that the AZO-TFP, BT-TFP, and MBT-TFP pairings had a D-A structure. Consequently, the COFs generated by AZO-TFP-BT-TFP and AZO-TFP-MBT-TFP exhibit a D1-A-D2-A structure. Additionally, D-A conjugation expanded HOMO level delocalization, which may improve inter-/intramolecular charge transmission and movement [74,75]. In addition, we conducted the DFT calculations to study the advantages of the D1-A-D2-A structure compared to the D-A structure. The isosurfaces of HOMO and LUMO of the AZO-TFP-BT-TFP and AZO-TFP-MBT-TFP units are shown in Fig. 3d, e. In both molecules, the HOMO is located on the donor part; the LUMO, on the other hand, is located on the acceptor part. These molecules show
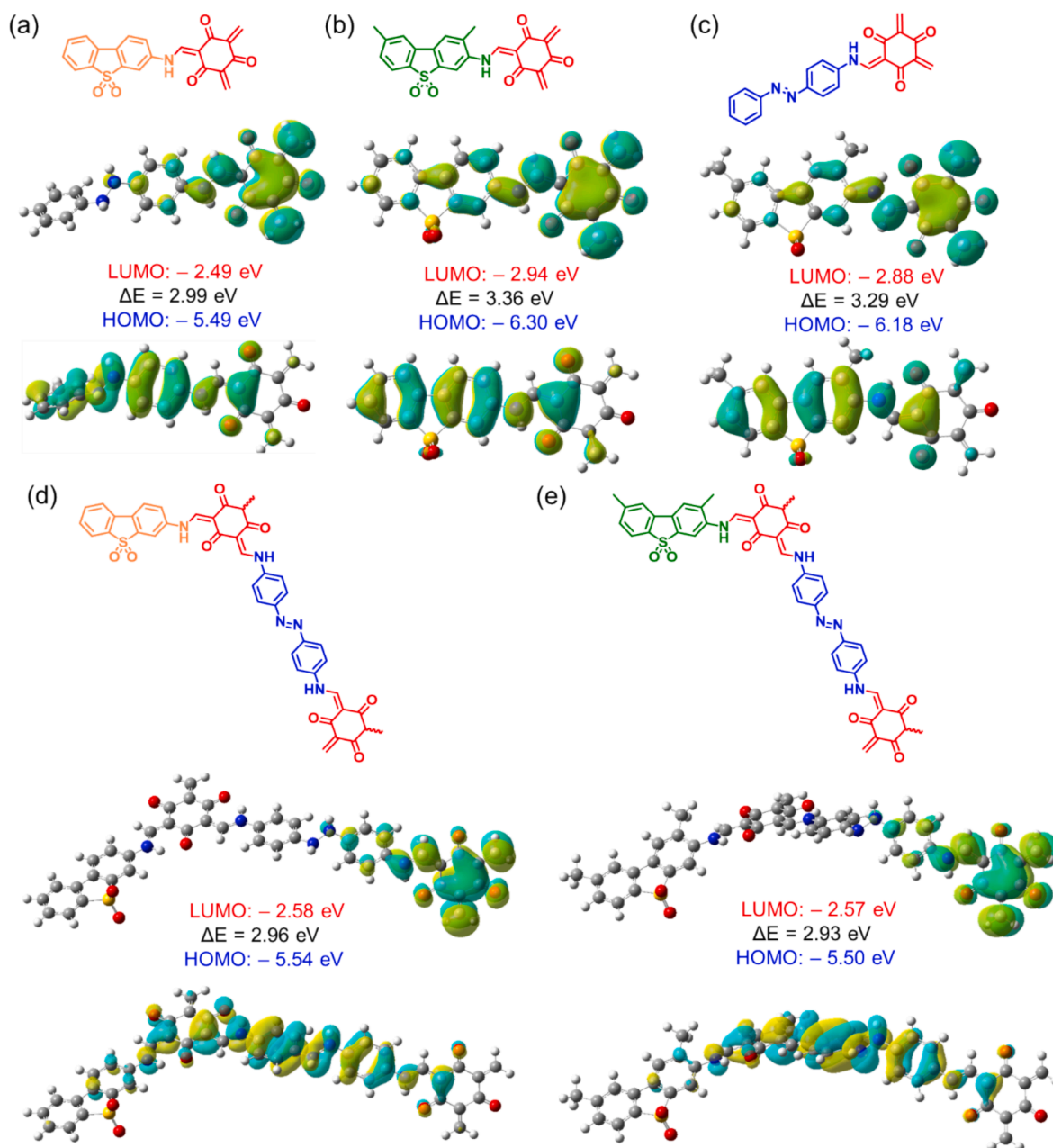
Fig. 3. HOMO and LUMO distribution of (a) BT-TFP, (b) MBT-TFP, (c) AZO-TFP, (d) BT-TFP-AZO-TFP, and (e) MBT-TFP-AZO-TFP units.

charge transfer upon excitation. As shown in Fig. 3a-e and S26, The D1-A-D2-A and COF units have a lower HOMO-LUMO energy gap than the D-A units; thus, the former are more reactive.

3.4. Photodegradation of dyes using COF photocatalysts

Considering the high surface area, excellent crystallinity, and orderly arranged, as well as narrow-band gaps of the as-prepared COFs, we assessed the photocatalytic performance of AZO-TFP-BT-TFP and AZO-TFP-MBT-TFP COFs in the degradation of organic pollutants, specifically the cationic organic dye Rhodamine B (RhB) and the anionic organic dye methyl orange (MO), in water under visible light irradiation (>450 nm). Over the control test, we observed the UV–Vis spectra of RhB and MO aqueous solutions without a photocatalyst. This proved that it was difficult to degrade RhB (25 mg L^{-1}, 60 mL) and MO (12.5 mg L^{-1}, 60 mL) under visible light for 4 h without a COF photocatalyst (Figures S27 and S28). Then, the efficiency of the COF photocatalyst (8

mg) in photodegradation was assessed using an aqueous solution of RhB (25 mg L^{-1}, 60 mL) or MO (12.5 mg L^{-1}, 60 mL). To reach adsorption–desorption equilibrium, the solution was agitated continuously in darkness for 60 min before being exposed to light. After 90 min of visible light irradiation, RhB dye photodegraded on COF at 76.47 ± 4.82 % for AZO-TFP-BT-TFP COF and 48.59 ± 1.12 % for AZO-TFP-MBT-TFP COF (Fig. 4a, S29, and S30). MO dye photodegraded at 75.78 ± 0.56 % for AZO-TFP-BT-TFP COF and 35.19 ± 2.81 % for AZO-TFP-MBT-TFP COF after 90 min of visible light exposure (Fig. 4b, S31, and S32). The AZO-TFP-BT-TFP and AZO-TFP-MBT-TFP COFs completely eliminated RhB molecules in 3.0 h for AZO-TFP-BT-TFP COF and in 3.5 h for AZO-TFP-MBT-TFP COF, achieving photodegradation efficiencies of 97.70 ± 0.51 % and 95.82 ± 0.61 % respectively (Fig. 4c). Conversely, the AZO-TFP-BT-TFP COF achieved full elimination of MO molecules in 3.0 h for AZO-TFP-BT-TFP COF, resulting in a photodegradation efficiency of 97.02 ± 2.54 % (Fig. 4d). The results suggest that the newly developed COFs have superior photocatalytic capabilities for decomposing cationic dyes
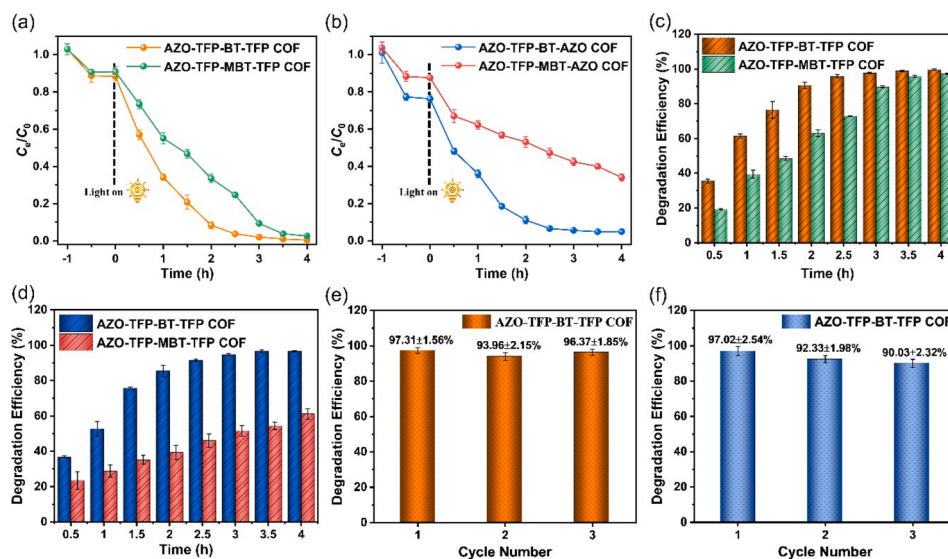
Fig. 4. Rates of photodegradation of an aqueous solution of (a) cationic RhB (25 mg L^{-1}, pH = 3) and (b) anionic MO (12.5 mg L^{-1}, pH = 3) onto AZO-TFP-BT-TFP (8 mg) and AZO-TFP-MBT-TFP (8 mg) COFs, measured at various periods of time. Photodegradation efficiencies of AZO-TFP-BT-TFP and AZO-TFP-MBT-TFP COFs for the degradation of (c) RhB and (d) MO in water under irradiation with visible light for various periods of time. Cycling the photocatalytic degradation of (e) RhB and (f) MO over AZO-TFP-BT-TFP COF in water. Each experiment was repeated three times.

compared to anionic dyes under visible light exposure. To verify this phenomenon, we conducted measurements of the Zeta potentials of the AZO-TFP-BT-TFP and AZO-TFP-MBT-TFP COFs. Figures S33 and S34 demonstrate that the zeta potentials of AZO-TFP-BT-TFP and AZO-TFP-MBT-TFP COFs exhibit negative charges of −20.4 and −24.6 mV, respectively. Therefore, the superior photocatalytic capabilities for decomposing cationic dyes compared to anionic dyes could be tentatively attributed to the stronger interaction between the electron-rich nitrogen (N–H and N=N) and oxygen (C=O and O=S=O) atoms in the COF skeletons with the cationic RhB molecules. In addition, Fig. 4a and 4b provided evidence for this hypothesis by showing that under the adsorption–desorption equilibrium (after stirring in the dark for 60 min), the AZO-TFP-BT-TFP and AZO-TFP-MBT-TFP COFs had adsorption capacities of 25 and 17.5 mg g^{-1}, respectively, for RhB dye molecules. In comparison, their adsorption capacities for MO dye molecules were 20.2 and 11.2 mg g^{-1}, respectively. Furthermore, the AZO-TFP-BT-TFP and AZO-TFP-MBT-TFP COFs exhibited similar band gaps. Consequently, the enhanced efficiency of RhB photodegradation observed with the AZO-TFP-BT-TFP COF, as compared to the AZO-TFP-MBT-TFP COF, can tentatively be ascribed to the more robust interaction between the AZO-TFP-BT-TFP COF and RhB molecules. The presence of the methyl group in the AZO-TFP-MBT-TFP COF hinders the interaction between the electron-rich N–H nitrogen atoms in the COF structure and the cationic RhB molecules. Furthermore, Fig. 4a supported this hypothesis by demonstrating that after being stirred in the dark for 60 min, the AZO-TFP-BT-TFP exhibited a higher RhB adsorption capacity of 25 mg g^{-1} under the adsorption–desorption equilibrium, whereas the AZO-TFP-MBT-TFP COF displayed lower RhB adsorption capacities of 17.5 mg g^{-1}. Our COF photocatalysts exhibited comparable or superior efficiency to various reported metal oxides, metal sulfides, COFs, and conjugated polymers in degrading RhB and MO under identical photocatalytic conditions (Tables S10 and S11). The conjugated polymers discussed earlier were synthesized using metal-catalyzed processes. In contrast, a simple and metal-free method for manufacturing AZO-TFP-BT-TFP and AZO-TFP-MBT-TFP COFs is detailed in our work. Moreover, the photocatalysts were used to study the mineralization of RhB and MO by employing total organic carbon (TOC). The data presented in Figure S35 demonstrates that the mineralization efficiency values for RhB molecules were 74.12 ± 1.45 % and 70.21 ± 0.97 % after 3.0 h for AZO-TFP-BT-TFP COF and 3.5 h for AZO-TFP-MBT-TFP COF,

respectively. On the other hand, the mineralization efficiency of MO molecules over AZO-TFP-BT-TFP and AZO-TFP-MBT-TFP COF reached values of 69.18 ± 1.56 % and 18.96 ± 2.12 %, respectively, during a time of 3.0 h. The mineralization and photocatalytic efficiency discrepancy relates to intermediates that may be mineralized in a longer reaction period.

Reusing and recycling were essential for economic usage and secondary pollution control. Thus, AZO-TFP-BT-TFP COF was tested for reusability in RhB and MO deterioration during three cycles under similar conditions. The AZO-TFP-BT-TFP COF maintained strong photocatalytic activity, reducing RhB by 1 % and MO by 7 % (Fig. 4e and 4f). To assess the stability of the AZO-TFP-BT-TFP COF photocatalyst, the powder of AZO-TFP-BT-TFP COF was separated after three cycles of RhB and MO degradation. Subsequently, measurements were taken using FTIR, ^{13}C ssNMR, XPS, PXRD, and FE-SEM techniques. No changes in intensity or position were detected in the FTIR, ^{13}C ssNMR, XPS, and PXRD peaks of AZO-TFP-BT-TFP COF after the prolonged photodegradation cycles, as shown in Figures S36A-D. Furthermore, the FE-SEM images demonstrated that the AZO-TFP-BT-TFP COF retained its characteristic curved fiber-like structures even after undergoing three cycles of RhB and MO degradation (Figures S36E-G). The results demonstrated the exceptional durability of our COF photocatalysts. The Langmuir-Hinshelwood model was applied to study COF photocatalytic degradation kinetics. Figures S37 and S38 confirm that both AZO-TFP-BT-TFP and AZO-TFP-MBT-TFP COFs exhibited pseudo-first-order reaction kinetics during the photodegradation processes of RhB and MO dyes. This is evident from the observation of strong linear fits when plotting −ln (C_o/C_t) against time (t). The reaction rate constants for the photodegradation of RhB were approximately 1.21 h^{-1} for the AZO-TFP-BT-TFP COF and 0.59 h^{-1} for the AZO-TFP-MBT-TFP (Table S12), while MO photodegradation reaction rate constants for the AZO-TFP-BT-TFP COF and the AZO-TFP-MBT-TFP were approximately 0.92 and 0.26 h^{-1} (Table S13).

After conducting the above investigations, it was determined that the AZO-TFP-BT-TFP COF is the most effective photocatalyst for the degradation of RhB and MO when exposed to visible light (>450 nm). Therefore, we selected the photocatalyst AZO-TFP-BT-TFP COF to investigate the impact of pH and catalyst dosage on photocatalytic degradation. The photocatalytic process can be significantly influenced by the pH of the solution, which is a critical environmental parameter
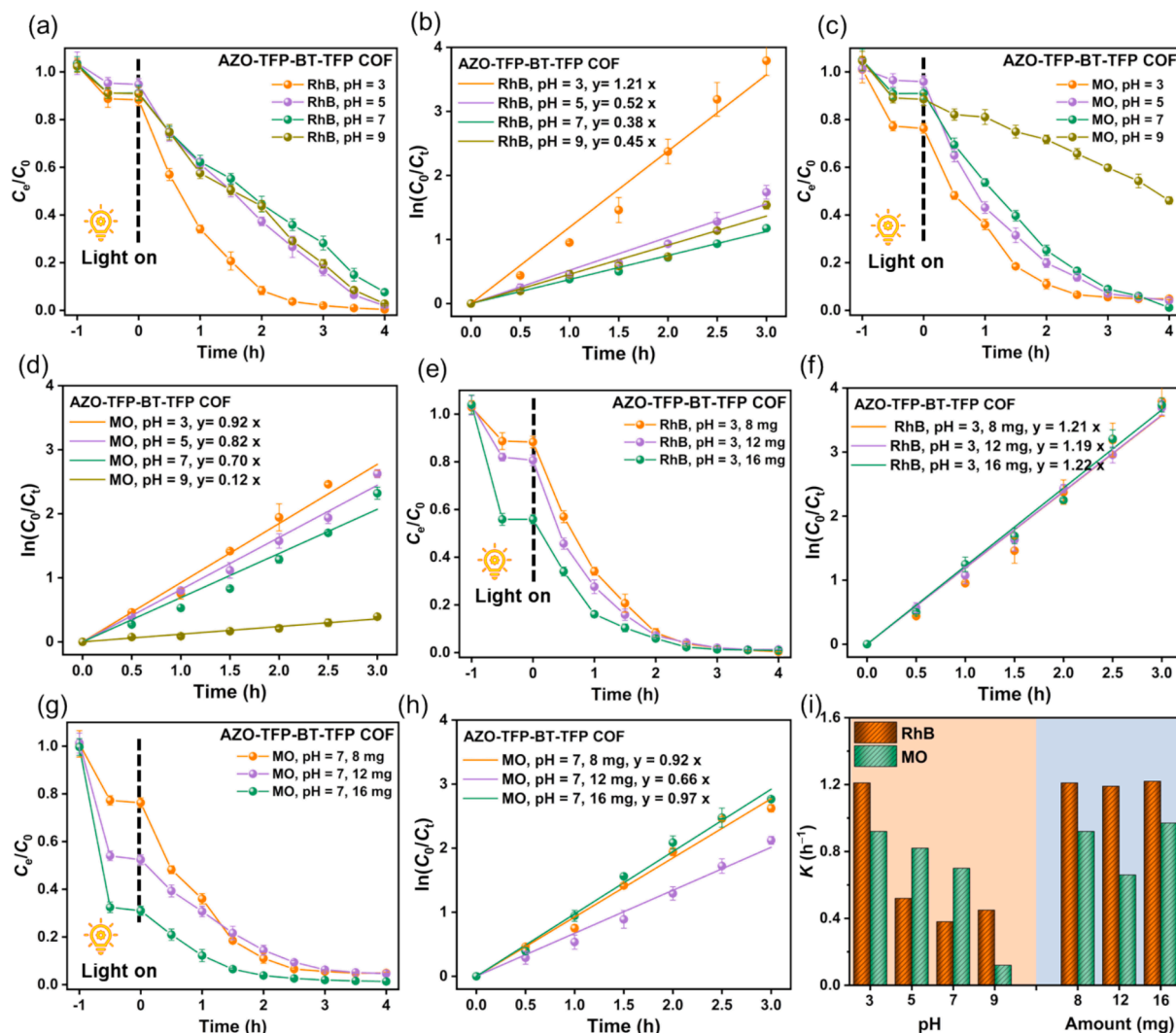
Fig. 5. (a–h) Rates of photodegradation of an aqueous solution of cationic RhB and anionic MO onto AZO-TFP-BT-TFP COF and the corresponding Pseudo-first-order kinetic curves under different conditions. (a,b) various values of pH (RhB: 25 mg L^{-1}; COF dosage: 8 mg). (c,d) various values of pH (MO: 12.5 mg L^{-1}; COF dosage: 8 mg). (e,f) various dosages of COF (RhB: 25 mg L^{-1}; pH: 3). (g,h) various dosages of COF (MO: 12.5 mg L^{-1}; pH: 3). (i) The corresponding reaction rate constant *k* of an aqueous solution of cationic RhB and anionic MO onto AZO-TFP-BT-TFP COF under different conditions. Each experiment was repeated three times.

[76]. The photodegradation effectiveness of AZO-TFP-BT-TFP COF (8 mg) for degrading a solution of RhB (25 mg L^{-1}, 60 mL) and MO (12.5 mg L^{-1}, 60 mL) under visible light was investigated at different pH levels (ranging from 3.0 to 9.0), as seen in Fig. 5a–d. The pH values can be tweaked by incorporating specific HCl or NaOH solutions. For the RhB dye, the AZO-TFP-BT-TFP COF showed the highest degradation performance and eliminated RhB molecules in 3.0 h at pH = 3.0, achieving photodegradation efficiencies of 97.70 ± 0.51 % (Fig. 5a and S39-42). Degradation performance is greater at lower pH solutions, with rate constants of 1.21, 0.52, 0.38, and 0.45 h^{-1} for pH = 3.0, 5.0, 7.0, and 9.0 (Fig. 5b). This higher photodegradation effectiveness of RhB over AZO-TFP-BT-TFP COF at pH = 3.0 can be attributed to the high concentration of Cl$^-$ ions and the presence of RhB in the cationic form. The higher Cl$^-$ concentration, at lower pH, may serve as a hole h^+ scavenger that accelerates the photodegradation reaction [77]. In addition, RhB may have two forms with distinct charges: cationic (RhBH$^+$) and zwitterion (RhB$^\pm$) (Figure S43). RhBH$^+$ is more prevalent at pH levels 1.0–3.0, whereas RhB$^\pm$ is more prevalent at pH levels over 4.0. RhB molecules are positively charged below pH 4.0, making electrostatic interaction with the negatively charged AZO-TFP-BT-TFP COF easier. RhB becomes zwitterionic in water with a pH over 4.0 [78]. Consequently, these zwitterionic forms face less ability to interact with the negatively

charged AZO-TFP-BT-TFP COF.

On the other hand, The AZO-TFP-BT-TFP COF exhibited the most effective degradation performance for MO dye, eliminating MO molecules in 3.0 h at pH = 3.0 and 5.0, attaining photodegradation efficiencies of 95.72 ± 0.59 and 95.98 ± 0.31 % (Fig. 5c and S44-47). The rate constants for pH values of 3.0, 5.0, 7.0, and 9.0 are computed to be 0.92, 0.82, 0.70, and 0.12 h^{-1}, respectively (Fig. 5d). This suggests that the degradation performance is lower in solutions with pH values of 3.0 and 5.0. The greater efficiency of MO compared to AZO-TFP-BT-TFP COF in degrading under the influence of light at pH = 3.0 and 5.0 may be ascribed to the high concentration of Cl$^-$ ions and the presence of MO in the zwitterion state. A larger concentration of Cl$^-$ ions at a lower pH may function as a scavenger for hole h^+ ions, so speeding up the photodegradation process. Furthermore, based on the available literature, MO may be found in two distinct forms with varying charges: the zwitterion (MOH$^\pm$) and anionic (MO$^-$) forms (Figure S48). MOH$^\pm$ is the predominant form in the pH range of 1.0–5.0, whereas MO$^-$ is more prevalent at pH values higher than 5.0. At a pH range of 1.0–5.0, MO ions are present in a zwitterionic state, which enhances their electrostatic interaction with the negatively charged AZO-TFP-BT-TFP COF. Conversely, when the pH of the aqueous solution exceeds 5.0, RhB undergoes a transformation into an anionic form. As a result, these
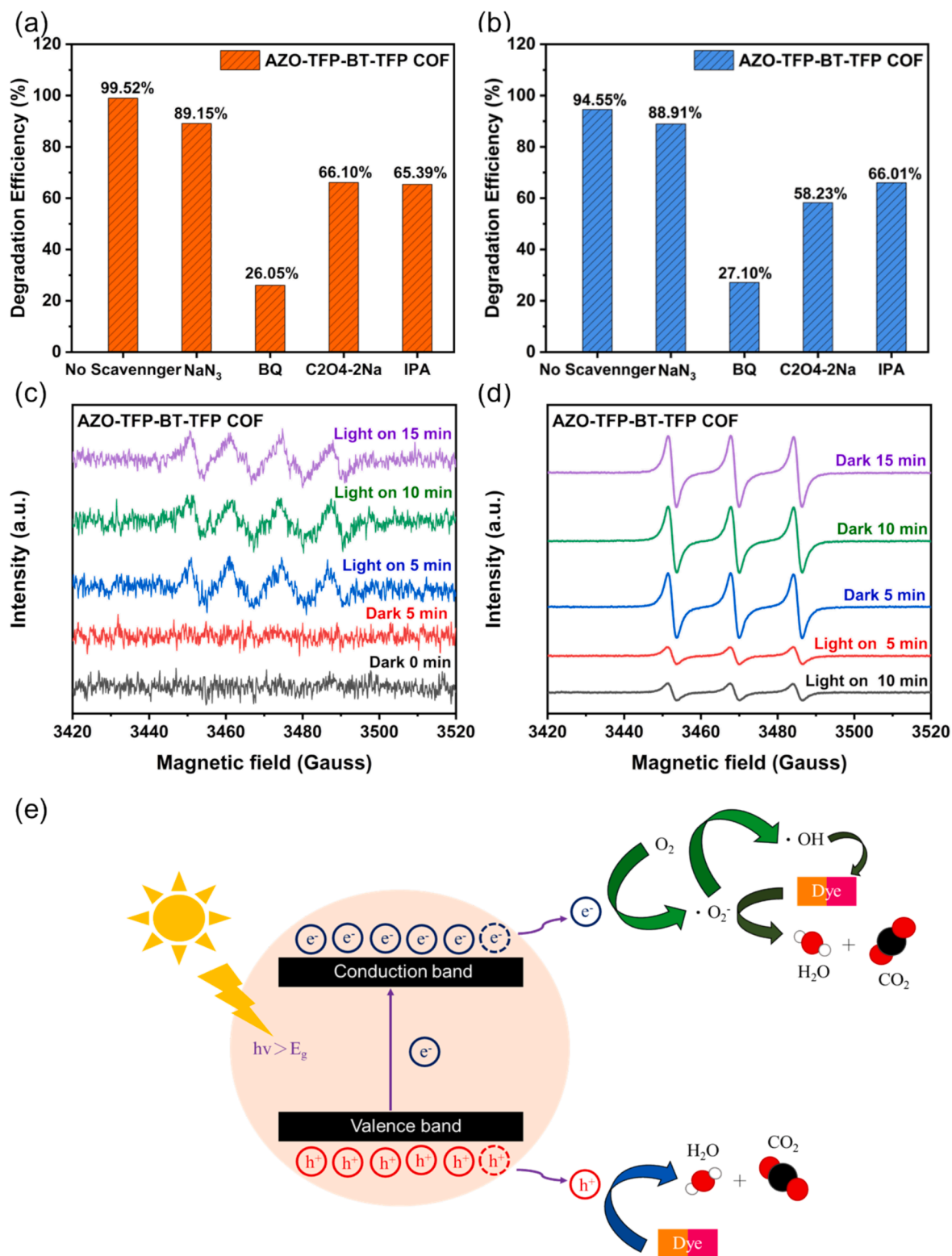
Fig. 6. (a) Effect of different scavengers on the photocatalytic degradation of (a) RhB (25 mg L^{-1}, pH = 3) and (b) MO (12.5 mg L^{-1}, pH = 3 by AZO-TFP-BT-TFP COF (8 mg) under visible light irradiation for 4 hr. EPR signals of (c) DMPO $^{\bullet}O_2^-$ and (d) TEMP h^+. (e) The proposed photocatalytic mechanism of AZO-TFP-BT-TFP COF for degradation under irradiation with visible light.

negatively charged forms encounter challenges while trying to interact with the AZO-TFP-BT-TFP COF, which also carries a negative charge. Hence, the most favorable pH for the degradation of RhB and MO by AZO-TFP-BT-TFP COF is 3.0.

Effective photocatalyst employment improves photocatalytic

efficiency. Fig. 5e-h show that catalyst dose significantly affects the breakdown rate of RhB and MO under visible light. The efficiency of AZO-TFP-BT-TFP COF in degrading a solution containing RhB (25 mg L^{-1}, 60 mL) and MO (12.5 mg L^{-1}, 60 mL) at pH = 3.0 under visible light was studied using various amounts of the catalyst (range from 8.0 to

16.0 mg). The degradation rate of the RhB dye by the AZO-TFP-BT-TFP COF remained almost constant when the dose of the photocatalyst was raised from 8.0 to 16.0 mg, as shown in Fig. 5e, S39, S49, and S50. The rate constants for catalyst doses of 8.0, 12.0, and 16.0 mg are determined to be 1.21, 1.19, and 1.22 h^{-1}, respectively (Fig. 5f). The consistent performance may be attributed to the accumulation of the photocatalyst in large doses, which obstructs the flow of light and reduces the number of active sites on the surface for absorbing photons [79,80]. On the other hand, the degradation rate of the MO dye by the AZO-TFP-BT-TFP COF is decreased when the dose of the photocatalyst is raised from 8.0 to 12.0 mg, as shown in Fig. 5g, S44, and S51. The rate constants for catalyst doses of 8.0 and 12.0 mg are determined to be 0.92 and 0.66 h^{-1}, respectively (Fig. 5h). Also, the decrease in performance may be ascribed to the clustering of the photocatalyst at high dosages, which hinders the penetration of light and diminishes the available sites for photon absorption on the surface. At a catalyst dose of 16 mg, almost 70 ± 0.19 % of the MO dye was adsorbed by the catalyst before the photodegradation reaction (Figure S52). Consequently, we discarded the excessive dose (16 mg) of catalyst. Hence, the most favorable pH and catalyst dosage for the degradation of RhB and MO by AZO-TFP-BT-TFP COF are 3.0 and 8.0 mg (Fig. 5i).

3.5. Effects of interfering substances on photodegradation

To assess prospective practical uses, the photodegradation effectiveness of AZO-TFP-BT-TFP COF was further investigated in the presence of various coexisting ions, different water samples, coexisting organic materials, and different contaminants. Usually, metal cations, including Na^+, Ca^{2+}, and Al^{3+}, exist in their stable oxidation states and hardly disrupt the photocatalytic process [81,82]. To investigate the impact of the mentioned cations on the degradation of RB, solutions of Na_2SO_4, $CaSO_4$, and $Al_2(SO4)_3$ with a concentration of 0.01 M were separately added to a solution containing RhB (25 mg L^{-1}, 60 mL, pH = 3.0) and MO (12.5 mg L^{-1}, 60 mL, pH = 3.0). The degradation process was performed under visible light using an AZO-TFP-BT-TFP COF with a mass of 8 mg. The photodegradation efficiencies of the AZO-TFP-BT-TFP COF for RhB dye were 85.32 ± 0.87, 77.56 ± 1.22, and 71.99 ± 0.69 % in the presence of Na^+, Ca^{2+}, and Al^{3+}, respectively, and for MO dye were 85.34 ± 1.87, 79.22 ± 1.65, and 77.65 ± 0.99 % in the presence of Na^+, Ca^{2+}, and Al^{3+}, respectively (Figure S53a). Al^{3+} showed the highest inhibition due to its propensity for binding to the AZO-TFP-BT-TFP COF anionic surface, inhibiting photodegradation sites due to its high charge density [83]. Additionally, Ca^{2+} inhibits degradation efficiency compared to Na^+ due to its larger charge density. Additionally, the effects of several inorganic anions were examined by adding 0.01 M of NaCl, Na_2CO_3, and Na_2SO_4 to a solution with RhB (25 mg L^{-1}, 60 mL, pH = 3.0) and MO (12.5 mg L^{-1}, 60 mL, pH = 3.0). The degrading method used 8 mg of AZO-TFP-BT-TFP COF under visible light. The photodegradation efficiencies of the AZO-TFP-BT-TFP COF for RhB dye were 96.12 ± 0.98, 63.25 ± 1.34, and 97.01 ± 0.65 % in the presence of Cl^-, CO_3^{2-}, and SO_4^{2-}, respectively, and for MO dye were 95.68 ± 1.82, 56.68 ± 1.21, and 97.02 ± 0.91 % in the presence of Cl^-, CO_3^{2-}, and SO_4^{2-}, respectively (Figure S53a). The Cl^- and SO_4^{2-} ions have minimal influence on the photodegradation efficiency of the AZO-TFP-BT-TFP COF. This is because these ions act as scavengers for hole $h+$ ions, thereby accelerating the photodegradation process [84]. On the other hand, the presence of CO_3^{2-} ion significantly reduces the photodegradation efficiency of the AZO-TFP-BT-TFP COF. This can be attributed to the increase in the pH of the solution to approximately 9.0, which slows down the photodegradation process [85].

The photodegradation efficacy of AZO-TFP-BT-TFP COF was investigated more thoroughly using various water samples, including tap water and mineral water, to assess its potential for practical use. As seen in Figure S53b, the mineral water was observed to achieve the optimum degradation efficiency of 90.11 ± 0.54 % for RB and 89.14 ± 0.99 % for MO under visible light. Meanwhile, the degradation efficiency dropped

to 80.54 ± 0.89 % for RB and 82.21 ± 1.22 % for MO in tap water. The primary cause of this phenomenon is the presence of dissolved organic compounds in tap water, as well as inorganic ions such as Ca^{2+}, Mg^{2+}, NO_3^-, and PO_4^- [86]. Consequently, the photocatalytic degradation ability is reduced. In addition, the efficiency of photodegradation of AZO-TFP-BT-TFP COF was examined utilizing different organic substances, such as humic acid, tannic acid, and lignin. The organic substance was dissolved in a 0.01 M NaOH solution to create 0.01 M solutions. Subsequently, the pH was modified to 7.0 by using a 0.01 M HCl solution. Adding three different organic matters inhibited the photodegradation of RhB and MO under visible light (Figure S53c). The photodegradation efficiencies of the AZO-TFP-BT-TFP COF for RhB dye were 77.54 ± 1.03, 75.11 ± 1.21, and 66.54 ± 0.87 % in the presence of humic acid, tannic acid, and lignin, respectively, and for MO dye were 74.12 ± 0.77, 70.08 ± 1.32, and 62.14 ± 0.98 % in the presence humic acid, tannic acid, and lignin, respectively (Figure S53c). The inhibitory impact of organic matter on photocatalysis may arise from the surface deactivation of AZO-TFP-BT-TFP COF via adsorption [87]. Nevertheless, the AZO-TFP-BT-TFP COF consistently shows promising outcomes under various circumstances, indicating its strong stability and practical effectiveness in removing organic contaminants from actual wastewater effluents.

The AZO-TFP-BT-TFP COF's photocatalytic efficiency was also evaluated for other comparable dye molecules often present in wastewater systems, namely methylene blue (MB) and Congo Red (CR), using the most favorable reaction conditions. According to Figure S53d, the degradation efficiencies of MB and CR were around 96.54 ± 1.02 % and 88.23 ± 0.87 %, respectively. Upon evaluating the degradation efficiency of the pollutants, it was discovered that the AZO-TFP-BT-TFP COF had the most superior degradation performance for RB dye under typical reaction circumstances.

3.6. Photodegradation mechanism and pathway

We examined the degradation mechanism of RhB and MO utilizing AZO-TFP-BT-TFP COF as a representative material while subjecting them to visible light irradiation. The process of photocatalytic degradation of organic pollutants produces many reactive species, such as Superoxide radicals ($^\bullet O_2^-$), photogenerated holes (h^+), Singlet oxygen ($^1O_2$), and hydroxyl radicals ($^\bullet OH$) [88]. Fig. 6a and 6b demonstrate that the removal rate of RhB and MO is considerably reduced to 26.05 and 27.10 %, respectively, by the addition of p-benzoquinone (BQ). This suggests that the primary free radical responsible for the photodegradation of RhB and MO is $^\bullet O_2^-$. In watery environments, electrons and dissolved O_2 form $^\bullet O_2^-$ [89]. The high photocurrent density of AZO-TFP-BT-TFP COF (Fig. 2d) matches its ability to create photoinduced electrons when exposed to visible light. Moreover, sodium azide (NaN_3) decreased degradation efficiency a little in RhB or MO solutions. Furthermore, incorporating sodium oxalate (C_2O_4-2Na) and isopropyl alcohol (IPA) reduced the photodegradation efficiencies of RhB to 66.10 and 65.39 %, respectively, and of MO to 58.23 and 66.01 %, suggesting that h^+ and $^\bullet OH$ species were also involved in the photodegradation of RhB and MO.

Electron paramagnetic resonance (EPR) experiments utilizing DMPO and TEMP are conducted in both dark and illuminated conditions to provide further evidence of the aforementioned active substance generation. The obtained ESR signals in Fig. 6c demonstrated that $^\bullet O_2^-$ is trapped in the DMPO [90]. The distinctive peaks for $^\bullet O_2^-$ are not detected when there is no exposure to light. In contrast, the associated peaks can be easily detected under light and their intensities increased with longer irradiation duration, confirming the presence of $^\bullet O_2^-$ radicals on the surface of AZO-TFP-BT-TFP COF. Simultaneously, the photogenerated h^+ could be trapped by TMPO to yield ESR signals [91]. Fig. 6d illustrates the detection of three distinct peaks of TMPO in the absence of light. However, these peaks noticeably diminished in intensity following exposure to light, providing evidence for the formation of TEMPO-h^+ spin adducts. Our attempt to detect the $^\bullet OH$ species using
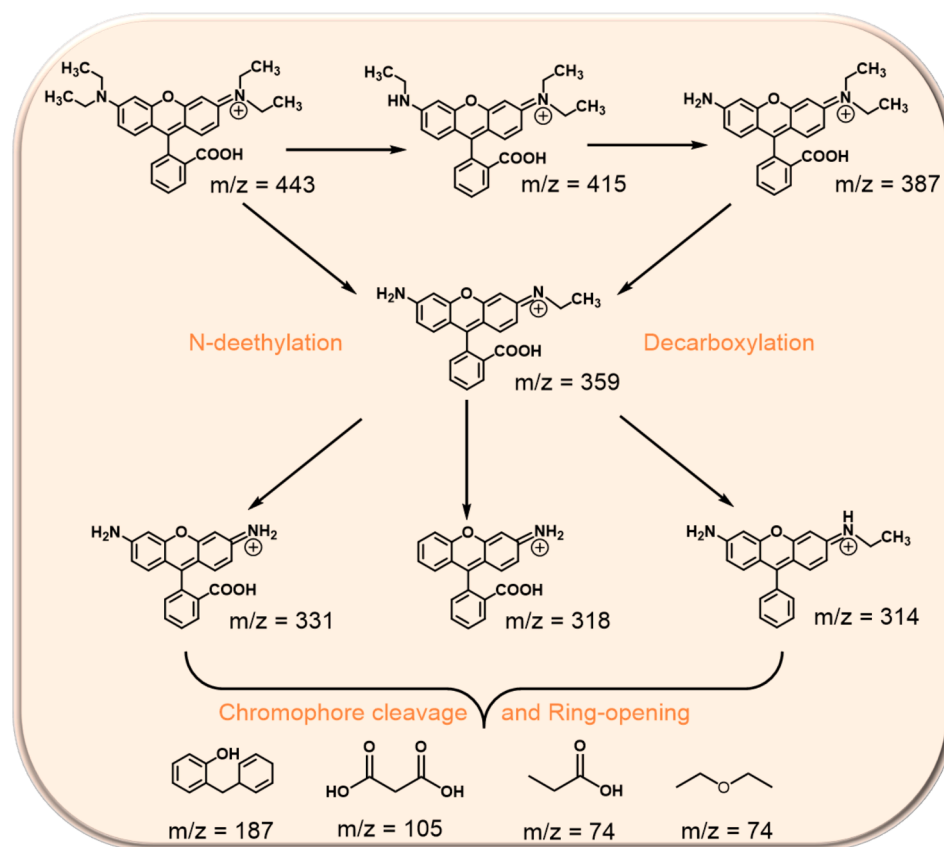
Scheme 2. Photodegradation pathways of RhB over the AZO-TFP-BT-TFP COF under irradiation with visible light.

EPR revealed a tiny peak intensity, suggesting that the $^{\bullet}OH$ species had a minimal role in the photodegradation of RhB and MO dyes (Figure S54a). In addition, the EPR analysis conducted to determine the presence of $^1O_2$ species did not exhibit any peaks, indicating that $^1O_2$ did not play a role in the photodegradation of RhB and MO dyes (Figure S54b). The data presented above confirms that the AZO-TFP-BT-TFP COF catalyst mostly generates h^+ and $^{\bullet}O_2^-$, with $^{\bullet}OH$ being produced to a lesser extent, when exposed to visible light.

Based on the findings, we conducted a comprehensive analysis of the AZO-TFP-BT-TFP COF to investigate the potential reactive radicals involved in its photodegradation. The hypothesized mechanism is shown in Fig. 6e. When exposed to light, electrons in AZO-TFP-BT-TFP COF are excited to their LUMO, whereas positive charges get fixed in their HOMO. The LUMO energy level of AZO-TFP-BT-TFP COF (-3.39 eV vs vacuum) is lower than the $O_2/^{\bullet}O_2^-$ potential (-4.17 eV vs vacuum) (Fig. 2c), suggesting that O_2 may react with AZO-TFP-BT-TFP COF to produce $^{\bullet}O_2^-$ radicals [92,93]. Remarkably, as compared to the $^{\bullet}OH/H_2O$ (-6.82 eV vs vacuum) [94], the HOMO potential in AZO-TFP-BT-TFP COF (-5.38 eV vs vacuum) is much lower. Thus, the photogenerated holes in the HOMO of AZO-TFP-BT-TFP COF exhibited significant oxidation ability and can be directly contributed to the photocatalytic destruction of RhB and MO [80]. Alternatively, the $^{\bullet}OH$ may also be generated by a two-electron oxidation process from the electrons in the LUMO, as shown by prior studies [95,96]. The activated oxygen molecule ($^{\bullet}O_2^-$) can be combined with electrons to create $^{\bullet}OH$ [97]. Following that, a credible outline of the route is shown below (equations 1–5).

$$H_2O \rightarrow H^+ + O_2 \tag{1}$$

$$e- + O_2 \rightarrow {}^{\bullet}O_2^- \tag{2}$$

$$e- + {}^{\bullet}O_2^- + H_2O \rightarrow {}^{\bullet}OH + OH^- \tag{3}$$

$$h+ + RhB\ (MO) \rightarrow cleavage\ of\ structures\ (CO_2 + H_2O) \tag{4}$$

$${}^{\bullet}O_2^-/{}^{\bullet}OH + RhB\ (MO) \rightarrow cleavage\ of\ structures\ (CO_2 + H_2O) \tag{5}$$
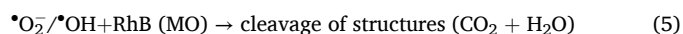
To confirm the chemical photodegradation routes of RhB and MO, the degraded products produced by AZO-TFP-BT-TFP COF when exposed to visible light are analyzed using HPLC-MS. The results of this analysis can be shown in Figures S55 and S56. During photocatalytic experiments, the degradation of the RhB dye was examined utilizing the AZO-TFP-BT-TFP COF catalyst. It was observed that as the duration of light exposure grew, the distinctive peak of RhB ($\lambda_{max} = 554$ nm) migrated towards shorter wavelengths, as shown in Figure S39. Observations reveal that during exposure to radiation for a duration of 0.5–1.5 h, there is a noticeable shift towards the blue end of the spectrum in the peak wavelength of 537 nm. This shift corresponds to N, N, N'-triethyl rhodamine, which has a maximum wavelength of 539 nm [98]. Following 2.5 h of exposure to light, two peaks were seen at wavelengths of 510 nm and 500 nm. These peaks corresponded to N-ethyl rhodamine and further deethylated rhodamine, with a maximum wavelength of 498 nm, respectively. The m/z values of 415, 387, 359, and 318 (Scheme 2) corresponded to the intermediate stages of the continuous deethylation process of RhB. The deamination and decarboxylation of the intermediate resulted in the production of m/z values of 331 and 314. Subsequently, the intermediates mentioned above were subjected to chromophore cleavage and ring-opening, resulting in the acquisition of m/z values of 187, 105, and 74. Ultimately, the intermediate substances underwent mineralization, resulting in the formation of tiny molecules such as H_2O and CO_2 (Scheme 2 and Figure S55). The distinctive peak of MO ($\lambda_{max} = 500$ nm) subtly shifted to a lower wavelength as the light duration increased in photocatalytic experiments of the degradation of the MO dye employing the AZO-TFP-BT-TFP COF catalyst (Figure S44). Mono- and di-demethylation intermediates of
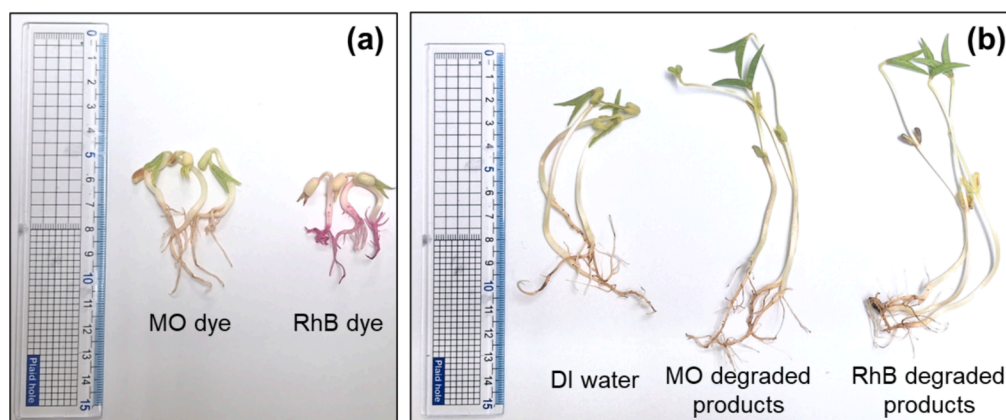
Fig. 7. The phytotoxicity test of the growth status of bean sprouts in (a) MO (12.5 mg L^{-1}) and RhB (25 mg L^{-1}) and (b) DI water, MO and RhB degraded products obtained after the complete photodegradation of RhB (25 mg L^{-1}, 60 mL, pH = 3) and MO (12.5 mg L^{-1}, 60 mL, pH = 3) solutions using the AZO-TFP-BT-TFP COF (8 mg) catalyst under visible light exposure.

MO were identified by the *m/z* values of 290 and 276, respectively. Then, the MO is subjected to mono-demethylation and hydroxylation to yield intermediates with a *m/z* value of 306, followed by demethylation to produce the intermediates with an *m/z* value of 292 (Scheme S6). After that, the intermediates were subjected to chromophore cleavage to provide intermediates with *m/z* values of 185, 189, 157, 124, and 106. Ultimately, the intermediates underwent mineralization, resulting in the formation of tiny molecules such as CO_2 and H_2O (Scheme S6-S8 and Figure S56).

3.7. Phytotoxicity evaluation

The phytotoxicity test has demonstrated efficacy in assessing the comparative toxicity and treatment effectiveness of dyes in wastewater [99]. Subsequently, the toxicity of the degraded products of RhB and MO, generated following the complete photodegradation of RhB (25 mg L^{-1}, 60 mL) and MO (12.5 mg L^{-1}, 60 mL) solutions using the AZO-TFP-BT-TFP COF catalyst under visible light exposure, was evaluated by the growth of bean sprouts. Fig. 7a and b illustrate the considerable heterogeneity in the effects of several treatments on plant seeds. The untreated RhB and MO impede the germination of mung beans and diminish stem length, indicating a signifying toxicity. On the other hand, mung beans grow well in the RhB and MO degraded products, showing that these substances are not harmful and that the produced organic small molecules help bean sprouts grow (Fig. 7b). The findings above underscore the efficacy of photocatalytic degradation utilizing our COF for ecologically sustainable and safe applications in actual wastewater treatment.

4. Conclusion

In summary, novel donor–acceptor β-ketoenamine-linked covalent organic frameworks– AZO-TFP-BT-TFP and AZO-TFP-MBT-TFP COFs– with a D1-A-D2-A structure were synthesized for photocatalytic degradation of organic chemical dyes. The COFs showed remarkable crystallinity, good thermal stability with a char output of up to 55 %, and a large surface area of up to 681 m^2/g. In addition, our COFs exhibited favorable band gap configuration, high conductivity, and effective charge transfer. Photocatalytic degradation of organic pollutants, specifically the cationic organic dye Rhodamine B and the anionic organic dye methyl orange, was accomplished with a notable degree of efficacy by both COFs. The COF photocatalysts demonstrated a remarkable level of efficacy, attaining 97.70 ± 0.51 %, accompanied by a reaction rate constant of 1.21 h^{-1}. The efficacy of these materials is comparable to, and may even exceed, that of numerous conjugated polymers and COFs that have been previously studied in analogous photodegradation

conditions. Our work, the first systematic study of incorporating the D1-A-D2-A structure in COFs, offered a design method for the strong degradation of organic contaminants employing stable photocatalysts.

CRediT authorship contribution statement

Yun-Zhen Xiao: Data curation, Investigation, Validation, Writing – review & editing. **Ahmed A.K. Mohammed:** Data curation, Investigation. **Shiao-Wei Kuo:** Conceptualization, Investigation, Resources, Validation, Visualization. **Ahmed F.M. EL-Mahdy:** Conceptualization, Data curation, Funding acquisition, Investigation, Project administration, Resources, Supervision, Validation, Visualization, Writing – review & editing.

Declaration of competing interest

The authors declare that they have no known competing financial interests or personal relationships that could have appeared to influence the work reported in this paper.

Data availability

Data will be made available on request.

Appendix A. Supplementary data

Supplementary data to this article can be found online at https://doi.org/10.1016/j.seppur.2024.129950.

References

[1] W.-T. Chung, I.M. Mekhemer, M.G. Mohamed, A.M. Elewa, A.F.M. EL-Mahdy, H.-H. Chou, S.-W. Kuo, K.C.-W. Wu, Recent advances in metal/covalent organic frameworks based materials: their synthesis, structure design and potential applications for hydrogen production, Coord. Chem. Rev. 483 (2023) 215066, https://doi.org/10.1016/j.ccr.2023.215066.

[2] Z. Shan, Y. Sun, M. Wu, Y. Zhou, J. Wang, S. Chen, R. Wang, G. Zhang, Metal-porphyrin-based three-dimensional covalent organic frameworks for electrocatalytic nitrogen reduction, Appl. Catal. B 342 (2024) 123418, https://doi.org/10.1016/j.apcatb.2023.123418.

[3] H.R. Abuzeid, A.F.M. EL-Mahdy, S.-W. Kuo, Covalent organic frameworks: design principles, synthetic strategies, and diverse applications, Giant 6 (2021) 100054, https://doi.org/10.1016/j.giant.2021.100054.

[4] A.F.M. EL-Mahdy, Y.H. Hung, T.H. Mansoure, H.H. Yu, T. Chen, S.W. Kuo, A hollow microtubular triazine-and benzobisoxazole-based covalent organic framework presenting sponge-like shells that functions as a high-performance supercapacitor, Chem. Asian. J. 14 (2019) 1429–1435, https://doi.org/10.1002/asia.201900296.

[5] T. Shan, H. Luo, S. Wu, J. Li, F. Zhang, H. Xiao, L. Huang, L. Chen, In situ formation of a covalent organic framework on g-C$_3$N$_4$ encapsulated with nanocellulosic carbon for enhanced photocatalytic N$_2$-to-NH$_3$ conversion, Fuel. 358 (2024) 130157, https://doi.org/10.1016/j.fuel.2023.130157.

[6] K.Y. Lin, A.F.M. EL-Mahdy, Covalent triazine frameworks based on triphenylpyridine building block for high-performance supercapacitor and selective CO$_2$ capture, Mater. Chem. Phys. 281 (2022) 125850, https://doi.org/10.1016/j.matchemphys.2022.125850.

[7] Q. Wang, Y. Tao, Z. Li, W. Ye, Y. Wang, D. Liu, Y. He, Visualizing dynamic competitive adsorption processes between iodine and methyl iodide within single covalent organic framework crystals, J. Hazard. Mater. 463 (2024) 132841, https://doi.org/10.1016/j.jhazmat.2023.132841.

[8] Q. Chang, H. Guo, Z. Shang, C. Zhang, Y. Zhang, G. Dong, B. Shen, J. Wang, Y. Zhang, PIM-based mixed matrix membranes containing covalent organic frameworks/ionic liquid composite materials for effective CO2/N2 separation, Sep. Purif. Technol. 330 (2024) 125518, https://doi.org/10.1016/j.seppur.2023.125518.

[9] A.F.M. EL-Mahdy, A.M. Elewa, S.W. Huang, H.H. Chou, S.W. Kuo, Dual-function fluorescent covalent organic frameworks: HCl sensing and photocatalytic H2 evolution from water, Adv. Opt. Mater. 8 (2020) 2000641, https://doi.org/10.1002/adom.202000641.

[10] A.F.M. EL-Mahdy, C.-H. Kuo, A. Alshehri, C. Young, Y. Yamauchi, J. Kim, S.-W. Kuo, Strategic design of triphenylamine-and triphenyltriazine-based two-dimensional covalent organic frameworks for CO$_2$ uptake and energy storage, J. Mater. Chem. A 6 (2018) 19532–19541, https://doi.org/10.1039/C8TA04781B.

[11] A.F.M. EL-Mahdy, M.-Y. Lai, S.-W. Kuo, A highly fluorescent covalent organic framework as a hydrogen chloride sensor: roles of Schiff base bonding and π-stacking, J. Mater. Chem. C 8 (2020) 9520–9528, https://doi.org/10.1039/D0TC01872D.

[12] H. Guo, J. Wang, Q. Fang, Y. Zhao, S. Gu, J. Zheng, Y. Yan, A quaternary-ammonium-functionalized covalent organic framework for anion conduction, CrystEngComm. 19 (2017) 4905–4910, https://doi.org/10.1039/C7CE00042A.

[13] Q. Fang, J. Wang, S. Gu, R.B. Kaspar, Z. Zhuang, J. Zheng, H. Guo, S. Qiu, Y. Yan, 3D porous crystalline polyimide covalent organic frameworks for drug delivery, J. Am. Chem. Soc. 137 (2015) 8352–8355, https://doi.org/10.1021/jacs.5b04147.

[14] L.R. Ahmed, L. Gilmanova, C.T. Pan, S. Kaskel, A.F.M. EL-Mahdy, Hollow spherical covalent organic frameworks from nonplanar or planar monomers for the fluorescence detection of telomere DNA: role of the 2-(2-azidoethoxy) ethoxy group, ACS Appl. Polym. Mater. 4 (2022) 9132–9143, https://doi.org/10.1021/acsapm.2c01460.

[15] L.R. Ahmed, C.H. Chuang, J. Luder, H.W. Yang, A.F.M. EL-Mahdy, Direct metal-free synthesis of uracil-and pentaazaphenalene-functionalized porous organic polymers via quadruple Mannich cyclization and their nucleobase recognition activities, Macromolecules 55 (2022) 10197–10209, https://doi.org/10.1021/acs.macromol.2c01627.

[16] Z. Chen, J. Wang, M. Hao, Y. Xie, X. Liu, H. Yang, G.I. Waterhouse, X. Wang, S. Ma, Tuning excited state electronic structure and charge transport in covalent organic frameworks for enhanced photocatalytic performance, Nat. Commun. 14 (2023) 1106, https://doi.org/10.1038/s41467-023-36710-x.

[17] M. Wu, Z. Shan, J. Wang, T. Liu, G. Zhang, Three-dimensional covalent organic framework with tty topology for enhanced photocatalytic hydrogen peroxide production, Chem. Eng. J. 454 (2023) 140121, https://doi.org/10.1016/j.cej.2022.140121.

[18] S. Liu, M. Wang, Y. He, Q. Cheng, T. Qian, C. Yan, Covalent organic frameworks towards photocatalytic applications: Design principles, achievements, and opportunities, Coord. Chem. Rev. 475 (2023) 214882, https://doi.org/10.1016/j.ccr.2022.214882.

[19] A.F.M. EL-Mahdy, H.A.E. Omr, Z.A. ALOthman, H. Lee, Design and synthesis of metal-free ethene-based covalent organic framework photocatalysts for efficient, selective, and long-term stable CO$_2$ conversion into methane, Colloid Interface Sci. 633 (2023) 775–785, https://doi.org/10.1016/j.jcis.2022.11.098.

[20] K.T. Tan, S. Ghosh, Z. Wang, F. Wen, D. Rodríguez-San-Miguel, J. Feng, N. Huang, W. Wang, F. Zamora, X. Feng, Covalent organic frameworks, Nat. Rev. Methods Primers. 3 (2023) 1, https://doi.org/10.1038/s43586-022-00181-z.

[21] G.-B. Wang, K.-H. Xie, H.-P. Xu, Y.-J. Wang, F. Zhao, Y. Geng, Y.-B. Dong, Covalent organic frameworks and their composites as multifunctional photocatalysts for efficient visible-light induced organic transformations, Coord. Chem. Rev. 472 (2022) 214774, https://doi.org/10.1016/j.ccr.2022.214774.

[22] B. Zhang, H. Mao, R. Matheu, J.A. Reimer, S.A. Alshmimri, S. Alshihri, O.M. Yaghi, Reticular synthesis of multinary covalent organic frameworks, J. Am. Chem. Soc. 141 (2019) 11420–11424, https://doi.org/10.1021/jacs.9b05626.

[23] A. Dey, F.A. Rahimi, S. Barman, A. Hazra, T.K. Maji, Metal-free 3D donor–acceptor COF with low exciton binding for solar fuel production based on CO$_2$ reduction, J. Mater. Chem. A 11 (2023) 13615–13622, https://doi.org/10.1039/D3TA00901G.

[24] Z. Li, T. Deng, S. Ma, Z. Zhang, G. Wu, J. Wang, Q. Li, H. Xia, S.-W. Yang, X. Liu, Three-component donor–π–acceptor covalent–organic frameworks for boosting photocatalytic hydrogen evolution, J. Am. Chem. Soc. 145 (2023) 8364–8374, https://doi.org/10.1021/jacs.2c11893.

[25] S. Barman, A. Singh, F.A. Rahimi, T.K. Maji, Metal-free catalysis: a redox-active donor–acceptor conjugated microporous polymer for selective visible-light-driven

[26] F.D. Wang, L.J. Yang, X.X. Wang, Y. Rong, L.B. Yang, C.X. Zhang, F.Y. Yan, Q.L. Wang, Pyrazine-functionalized donor-acceptor covalent organic frameworks for enhanced photocatalytic H$_2$ evolution with high proton transport, Small 19 (2023) 2207421, https://doi.org/10.1002/smll.202207421.

[27] C. Cui, X. Zhao, X. Su, N. Xi, X. Wang, X. Yu, X.L. Zhang, H. Liu, Y. Sang, Porphyrin-based donor-acceptor covalent organic polymer/ZnIn$_2$S$_4$ Z-scheme heterostructure for efficient photocatalytic hydrogen evolution, Adv. Funct. Mater. 32 (2022) 2208962, https://doi.org/10.1002/adfm.202208962.

[28] G.-B. Wang, H.-P. Xu, K.-H. Xie, J.-L. Kan, J. Fan, Y.-J. Wang, Y. Geng, Y.-B. Dong, A covalent organic framework constructed from a donor–acceptor–donor motif monomer for photocatalytic hydrogen evolution from water, J. Mater. Chem. A 11 (2023) 4007–4012, https://doi.org/10.1039/D2TA09625K.

[29] H. Yu, J. Zhang, X. Yan, C. Wu, X. Zhu, B. Li, T. Li, Q. Guo, J. Gao, M. Hu, Donor–acceptor covalent organic framework hollow submicrospheres with a hierarchical pore structure for visible-light-driven H$_2$ evolution, J. Mater. Chem. A 10 (2022) 11010–11018, https://doi.org/10.1039/D2TA01058E.

[30] W. Huang, Y. Hu, Z. Qin, Y. Ji, X. Zhao, Y. Wu, Q. He, Y. Li, C. Zhang, J. Lu, Highly crystalline and water-wettable benzobisthiazole-based covalent organic frameworks for enhanced photocatalytic hydrogen production, Natl. Sci. Rev. 10 (2023) nwac171, https://doi.org/10.1093/nsr/nwac171.

[31] Q. Liao, W. Xu, X. Huang, C. Ke, Q. Zhang, K. Xi, J. Xie, Donor-acceptor type [4+ 3] covalent organic frameworks: sub-stoichiometric synthesis and photocatalytic application, Sci China Chem. 63 (2020) 707–714, https://doi.org/10.1007/s11426-019-9696-3.

[32] J. Swain, A. Priyadarshini, S. Hajra, S. Panda, J. Panda, R. Samantaray, Y. Yamauchi, M. Han, H.J. Kim, R. Sahu, Photocatalytic dye degradation by BaTiO$_3$/zeolitic imidazolate framework composite, J. Alloys Compd. 965 (2023) 171438, https://doi.org/10.1016/j.jallcom.2023.171438.

[33] M. Fan, J. Hu, R. Cao, W. Ruan, X. Wei, A review on experimental design for pollutants removal in water treatment with the aid of artificial intelligence, Chemosphere. 200 (2018) 330–343, https://doi.org/10.1016/j.chemosphere.2018.02.111.

[34] L. Huang, M. He, B. Chen, B. Hu, Magnetic Zr-MOFs nanocomposites for rapid removal of heavy metal ions and dyes from water, Chemosphere 199 (2018) 435–444, https://doi.org/10.1016/j.chemosphere.2018.02.019.

[35] S. Li, M. Cai, C. Wang, Y. Liu, N. Li, P. Zhang, X. Li, Rationally designed Ta3N5/BiOCl S-scheme heterojunction with oxygen vacancies for elimination of tetracycline antibiotic and Cr (VI): performance, toxicity evaluation and mechanism insight, J. Mater. Sci. Technol. 123 (2022) 177–190, https://doi.org/10.1016/j.jmst.2022.02.012.

[36] F. Wei, H. Xing, Z. Xiu, J. Li, D. Xing, X. Han, Z-scheme TiO2-Au@ CN heterojunction for simultaneous water purification of disinfection and organic pollutant removal by simulated solar light, Mater. Res. Bull. 168 (2023) 112450, https://doi.org/10.1016/j.materresbull.2023.112450.

[37] S. Li, M. Cai, Y. Liu, C. Wang, K. Lv, X. Chen, S-Scheme photocatalyst TaON/Bi2WO6 nanofibers with oxygen vacancies for efficient abatement of antibiotics and Cr (VI): Intermediate eco-toxicity analysis and mechanistic insights, Chinese J. Catal. 43 (2022) 2652–2664, https://doi.org/10.1016/S1872-2067(22)64106-8.

[38] F.A. Qaraah, S.A. Mahyoub, A. Hezam, A. Qaraah, Q.A. Drmosh, G. Xiu, Construction of 3D flowers-like O-doped g-C3N4-[N-doped Nb2O5/C] heterostructure with direct S-scheme charge transport and highly improved visible-light-driven photocatalytic efficiency, Chinese J. Catal. 43 (2022) 2637–2651, https://doi.org/10.1016/S1872-2067(21)64038-X.

[39] J.H. Wang, T.A. Gaber, S.W. Kuo, A. f. m., EL-Mahdy, π-electron-extended triazine-based covalent organic framework as photocatalyst for organic pollution degradation and H$_2$ production from water, Polymers 15 (2023) 1685, https://doi.org/10.3390/polym15071685.

[40] G.V. Serban, V.I. Iancu, C. Dinu, A. Tenea, N. Vasilache, I. Cristea, M. Niculescu, I. Ionescu, F.L. Chiriac, Removal efficiency and adsorption kinetics of methyl orange from wastewater by commercial activated carbon, Sustainability 15 (2023) 12939, https://doi.org/10.3390/su151712939.

[41] S.S. Imam, H.F. Babamale, A short review on the removal of rhodamine B dye using agricultural waste-based adsorbents, Asian J. Chem. Sci. 7 (2020) 25–37, https://doi.org/10.9734/ajocs/2020/v7i119013.

[42] L. Wang, J. Wang, M. Zhao, Kinetic studies on electrochemical degradation of rhodamine B, J. Water Chem. Technol. 43 (2021) 123–130, https://doi.org/10.3103/S1063455X21020132.

[43] R.H. Waghchaure, V.A. Adole, B.S. Jagdale, Photocatalytic degradation of methylene blue, rhodamine B, methyl orange and Eriochrome black T dyes by modified ZnO nanocatalysts: a concise review, Inorg. Chem. Commun. 143 (2022) 109764, https://doi.org/10.1016/j.inoche.2022.109764.

[44] A.S. Barreto, K.O. Moura, M.D.C.S. Barreto, S.A. Júnior, Luminescence of rare earth 3D hydroxide framework Eu3+-doped and its application in dye adsorption tests, Appl. Clay Sci. 245 (2023) 107128, https://doi.org/10.1016/j.clay.2023.107128.

[45] Y. Zhang, G. Luo, Q. Wang, Y. Zhang, M. Zhou, Kinetic study of the degradation of rhodamine B using a flow-through UV/electro-Fenton process with the presence of ethylenediaminetetraacetic acid, Chemosphere 240 (2020) 124929, https://doi.org/10.1016/j.chemosphere.2019.124929.

[46] A.A. Al-Gheethi, Q.M. Azhar, P.S. Kumar, A.A. Yusuf, A.K. Al-Buriahi, R.M.S. R. Mohamed, M.M. Al-Shaibani, Sustainable approaches for removing Rhodamine B dye using agricultural waste adsorbents: a review, Chemosphere 287 (2022) 132080, https://doi.org/10.1016/j.chemosphere.2021.132080.

CO$_2$ reduction to CH$_4$, J. Am. Chem. Soc. 143 (2021) 16284–16292, https://doi.org/10.1021/jacs.1c07916.

[47] T.O. Ajiboye, O.A. Oyewo, D.C. Onwudiwe, Adsorption and photocatalytic removal of Rhodamine B from wastewater using carbon-based materials, FlatChem. 29 (2021) 100277, https://doi.org/10.1016/j.flatc.2021.100277.

[48] M. Ikram, M. Naeem, M. Zahoor, M.M. Hanafiah, A.A. Oyekanmi, R. Ullah, D.A. A. Farraj, M.S. Elshikh, I. Zekker, N. Gulfam, Biological degradation of the azo dye basic orange 2 by Escherichia coli: A sustainable and ecofriendly approach for the treatment of textile wastewater, Water 14 (2022) 2063, https://doi.org/10.3390/w14132063.

[49] S. Dutta, J. Bhattacharjee, Development in wastewater treatment research and processes, Elsevier, 2022, pp. 1–21.

[50] M. Harja, G. Buema, D. Bucur, Recent advances in removal of Congo Red dye by adsorption using an industrial waste, Sci. Rep. 12 (2022) 6087, https://doi.org/10.1038/s41598-022-10093-3.

[51] M. G. Kotp, C.-L. Chang and A. F. M. EL-Mahdy, etraphenyl-p-phenylenediamine-based tunable conjugated microporous polymers: Adsorption and photodegradation of hazardous dyestuff in aqueous environments, J. Water Process. Eng. 53 (2023) 103675, doi: 10.1016/j.jwpe.2023.103675.

[52] H. Shirzadi, A. Nezamzadeh-Ejhieh, An efficient modified zeolite for simultaneous removal of Pb (II) and Hg (II) from aqueous solution, J. Mol. Liq. 230 (2017) 221–229, https://doi.org/10.1016/j.molliq.2017.01.029.

[53] A. Nezamzadeh-Ejhieh, M. Karimi-Shamsabadi, Decolorization of a binary azo dyes mixture using CuO incorporated nanozeolite-X as a heterogeneous catalyst and solar irradiation, Chem. Eng. J. 228 (2013) 631–641, https://doi.org/10.1016/j.cej.2013.05.035.

[54] Y. Wu, L. Chen, X. Long, X. Zhang, B. Pan, J. Qian, Multi-functional magnetic water purifier for disinfection and removal of dyes and metal ions with superior reusability, J. Hazard. Mater. 347 (2018) 160–167, https://doi.org/10.1016/j.jhazmat.2017.12.037.

[55] M. Fan, P. Zhang, C. Wang, H. Sun, Highly efficient removal of ionic dyes in aqueous solutions using magnetic 3D reduced graphene oxide aerogel supported nano zero-valent iron, Environ. Eng. Res. 29 (2024), https://doi.org/10.4491/eer.2023.149.

[56] C.A. Mbachu, A.K. Babayemi, T.C. Egbosiuba, J.I. Ike, I.J. Ani, S. Mustapha, Green synthesis of iron oxide nanoparticles by Taguchi design of experiment method for effective adsorption of methylene blue and methyl orange from textile wastewater, RINENG 19 (2023) 101198, https://doi.org/10.1016/j.rineng.2023.101198.

[57] Z.T. Chong, L.S. Soh, W.F. Yong, Valorization of agriculture wastes as biosorbents for adsorption of emerging pollutants: Modification, remediation and industry application, RINENG 17 (2023) 100960, https://doi.org/10.1016/j.rineng.2023.100960.

[58] A.F.M. EL-Mahdy, M.B. Zakaria, H.-X. Wang, T. Chen, Y. Yamauchi, S.-W. Kuo, Heteroporous bifluorenylidene-based covalent organic frameworks displaying exceptional dye adsorption behavior and high energy storage, J. Mater. Chem. A 8 (2020) 25148–25155, https://doi.org/10.1039/D0TA07281H.

[59] A. F. M. EL-Mahdy, T.-E. Liu and S.-W. Kuo, Direct synthesis of nitrogen-doped mesoporous carbons from triazine-functionalized resol for CO2 uptake and highly efficient removal of dyes, J. Hazard. Mater. 391 (2020) 122163, doi: 10.1016/j.jhazmat.2020.122163.

[60] J. Xue, E. Zhu, H. Zhu, D. Liu, H. Cai, C. Xiong, Q. Yang, Z. Shi, Dye adsorption performance of nanocellulose beads with different carboxyl group content, Cellulose 30 (2023) 1623–1636, https://doi.org/10.21203/rs.3.rs-1995882/v1.

[61] A.I. Osman, E.M.A. E.M.A. El-Monaem, A.M. Elgarahy, C.O. Aniagor, M. Hosny, M. Farghali, E. Rashad, M.I. Ejimofor, E.A. López-Maldonado, I. Ihara, Methods to prepare biosorbents and magnetic sorbents for water treatment: a review, Environ. Chem. Lett. 21 (2023) 2337–2398, https://doi.org/10.1007/s10311-023-01603-4.

[62] S. Lu, Y. Ma, L. Zhao, Production of ZnO-CoOx-CeO2 nanocomposites and their dye removal performance from wastewater by adsorption-photocatalysis, J. Mol. Liq. 364 (2022) 119924, https://doi.org/10.1016/j.molliq.2022.119924.

[63] A. Rafiq, M. Ikram, S. Ali, F. Niaz, M. Khan, Q. Khan, M. Maqbool, Photocatalytic degradation of dyes using semiconductor photocatalysts to clean industrial water pollution, J. Ind. Eng. Chem. 97 (2021) 111–128, https://doi.org/10.1016/j.jiec.2021.02.017.

[64] Y. Zhuang, Q. Zhu, G. Li, Z. Wang, P. Zhan, C. Ren, Z. Si, S. Li, D. Cai, P. Qin, Photocatalytic degradation of organic dyes using covalent triazine-based framework, Mater. Res. Bull. 146 (2022) 111619, https://doi.org/10.1016/j.materresbull.2021.111619.

[65] A. Saber, C.-C. Chueh, M. Rashad, S.-W. Kuo, A. EL-Mahdy, hiazolyl-linked conjugated microporous polymers for enhancement adsorption and photocatalytic degradation of organic dyes from water, Mater. Today Sustain. 23 (2023) 100429, https://doi.org/10.1016/j.mtsust.2023.100429.

[66] S. Ruidas, A. Chowdhury, A. Ghosh, A. Ghosh, S. Mondal, A.D. Wonanke, M. Addicoat, A.K. Das, A. Modak, A. Bhaumik, Covalent organic framework as a metal-free photocatalyst for dye degradation and radioactive iodine adsorption, Langmuir 39 (2023) 4071–4081, https://doi.org/10.1021/acs.langmuir.2c03379.

[67] Q. Wang, M. Unno, H. Liu, Organic–inorganic hybrid near-infrared emitting porous polymer for detection and photodegradation of antibiotics, ACS Sustain. Chem. Eng. 10 (2022) 7309–7320, https://doi.org/10.1021/acssuschemeng.2c00935.

[68] S. Mushtaq, S. Bi, F. Zhang, M.M. Naseer, Fully unsaturated all-carbon bifluorenylidene-based polymeric frameworks: synthesis and efficient photocatalysis, New J. Chem. 45 (2022) 17374–17385, https://doi.org/10.1039/D2NJ02405E.

[69] W. K. An, S. J. Zheng, X. Xu, L. J. Liu, J. S. Ren, L. Fan, Z. K. Yang, Y. Ren and C. Xu Integrating benzofuran and heteroradialene into donor-acceptor covalent organic frameworks for photocatalytic construction of multi-substituted olefins, Appl. Catal. B. 316 (2022) 121630, doi: 10.1016/j.apcatb.2022.121630.

[70] A.F.M. EL-Mahdy, F.W. Lin, W.H. Su, T. Chen, S.W. Kuo, Photoresponsive azobenzene materials based on pyridine-functionalized benzoxazines as surface relief gratings, ACS Appl. Polym. Mater. 2 (2019) 791–804, https://doi.org/10.1021/acsapm.9b01079.

[71] X. Wang, L. Chen, S.Y. Chong, M.A. Little, Y. Wu, W.H. Zhu, R. Clowes, Y. Yan, M. A. Zwijnenburg, R.S. Sprick, A.I. Cooper, Sulfone-containing covalent organic frameworks for photocatalytic hydrogen evolution from water, Nat. Chem. 10 (2018) 1180–1189, https://doi.org/10.1038/s41557-018-0141-5.

[72] E. Zhu, G. Ge, J. Shu, M. Yi, L. Bian, J. Hai, J. Yu, Y. Liu, J. Zhou, W. Tang, Direct access to 4, 8-functionalized benzo [1, 2-b: 4, 5-b'] dithiophenes with deep low-lying HOMO levels and high mobilities, J. Mater. Chem. A 2 (2014) 13580–13586, https://doi.org/10.1039/C4TA01226G.

[73] C. Wang, F. Zheng, L. Zhang, J. Yang, P. Dong, Insight into the role of graphene quantum dots on the boosted photocatalytic H2 production performance of a covalent organic framework, Appl. Surf. Sci. 640 (2023) 158383, https://doi.org/10.1016/j.apsusc.2023.158383.

[74] H. Yao, L. Ye, H. Zhang, S. Li, S. Zhang, J. Hou, Molecular design of benzodithiophene-based organic photovoltaic materials, Chem. Rev. 116 (2016) 7397–7457, https://doi.org/10.1021/acs.chemrev.6b00176.

[75] A.F. Saber, A.M. Elewa, H.H. Chou, A.f.m., EL-Mahdy, Donor-acceptor carbazole-based conjugated microporous polymers as photocatalysts for visible-light-driven H2 and O2 evolution from water splitting, Appl. Catal. B: Environ. 316 (2022) 121624, https://doi.org/10.1016/j.apcatb.2022.121624.

[76] H. Shi, H. Zhu, T. Jin, L. Chen, J. Zhang, K. Qiao, Z. Chen, Construction of Bi/Polyoxometalate doped TiO2 composite with efficient visible-light photocatalytic performance: mechanism insight, degradation pathway and toxicity evaluation, Appl. Surf. Sci. 615 (2023) 156310, https://doi.org/10.1016/j.apsusc.2022.156310.

[77] Y. Shi, L. Luo, Y. Zhang, Y. Chen, S. Wang, L. Li, Y. Long, F. Jiang, Synthesis and characterization of α/β-Bi2O3 with enhanced photocatalytic activity for 17α-ethynylestradiol, Ceram. Int. 43 (2017) 7627–7635, https://doi.org/10.1016/j.ceramint.2017.03.057.

[78] A.V. Deshpande, U. Kumar, Effect of method of preparation on photophysical properties of Rh-B impregnated sol–gel hosts, J. Non-Crystalline Solids 306 (2002) 149–159, https://doi.org/10.1016/S0022-3093(02)01054-2.

[79] K. Gurung, M.C. Ncibi, S.K. Thangaraj, J. Jänis, M. Seyedsalehi, M. Sillanpää, Removal of pharmaceutically active compounds (PhACs) from real membrane bioreactor (MBR) effluents by photocatalytic degradation using composite Ag2O/P-25 photocatalyst, Sep. Purif. Technol. 215 (2019) 317–328, https://doi.org/10.1016/j.seppur.2018.12.069.

[80] N. Srinivasan, M. Anbuchezhiyan, S. Harish, S. Ponnusamy, Efficient catalytic activity of BiVO4 nanostructures by crystal facet regulation for environmental remediation, Chemosphere 289 (2022) 133097, https://doi.org/10.1016/j.chemosphere.2021.133097.

[81] S. Raha, M. Ahmaruzzaman, Enhanced performance of a novel superparamagnetic g-C3N4/NiO/ZnO/Fe3O4 nanohybrid photocatalyst for removal of esomeprazole: effects of reaction parameters, co-existing substances and water matrices, Chem. Eng. J. 395 (2020) 124969, https://doi.org/10.1016/j.cej.2020.124969.

[82] Y. Zhang, Y. Xiao, Y. Zhong, T.T. Lim, Comparison of amoxicillin photodegradation in the UV/H2O2 and UV/persulfate systems: reaction kinetics, degradation pathways, and antibacterial activity, Chem. Eng. J. 372 (2019) 420–428, https://doi.org/10.1016/j.cej.2019.04.160.

[83] D.E. Santiago, J. Araña, O. González-Díaz, M.E. Alemán-Dominguez, A.C. Acosta-Dacal, C. Fernandez-Rodríguez, J. Pérez-Peña, J.M. Doña-Rodríguez, Effect of inorganic ions on the photocatalytic treatment of agro-industrial wastewaters containing imazalil, Appl. Catal. B Environ. 156 (2014) 284–292, doi: 10.1016/j.apcatb.2014.03.022.

[84] H. Gao, S. Yan, J. Wang, Z. Zou, Inorganic ions promoted photocatalysis based on polymer photocatalyst, Appl. Catal. B Environ. 158 (2014) 321–328, https://doi.org/10.1016/j.apcatb.2014.04.036.

[85] Q. He, C. Xie, D. Gan, C. Xiao, The efficient degradation of organic pollutants in an aqueous environment under visible light irradiation by persulfate catalytically activated with kaolin-Fe2O3, RSC Adv. 10 (2020) 43–52, https://doi.org/10.1039/C9RA09253F.

[86] F. Chen, Q. Yang, Y. Wang, J. Zhao, D. Wang, X. Li, Z. Guo, H. Wang, Y. Deng, C. Niu, G. Zeng, Novel ternary heterojunction photococatalyst of Ag nanoparticles and g-C3N4 nanosheets co-modified BiVO4 for wider spectrum visible-light photocatalytic degradation of refractory pollutant, Appl. Catal., B 205 (2017) 133–147, https://doi.org/10.1016/j.apcatb.2016.12.017.

[87] D. Awfa, M. Ateia, M. Fujii, C. Yoshimura, Photocatalytic degradation of organic micropollutants: Inhibition mechanisms by different fractions of natural organic matter, Water Res. 174 (2020) 115643, https://doi.org/10.1016/j.watres.2020.115643.

[88] J.H. Wang, C.L. Chang, Z.W. Zhang, A.F.M. EL-Mahdy, Facile metal-free synthesis of pyrrolo [3, 2-b] pyrrolyl-based conjugated microporous polymers for high-performance photocatalytic degradation of organic pollutants, Polym. Chem. 13 (2022) 5300–5308, https://doi.org/10.1039/D2PY00658H.

[89] W. Li, Z. Wang, Y. Li, J.B. Ghasemi, J. Li, G. Zhang, Visible-NIR light-responsive 0D/2D CQDs/Sb2WO6 nanosheets with enhanced photocatalytic degradation performance of RhB: unveiling the dual roles of CQDs and mechanism study, J. Hazard. Mater. 424 (2022) 127595, https://doi.org/10.1016/j.jhazmat.2021.127595.

[90] X. Yang, L. Tian, X. Zhao, H. Tang, Q. Liu, G. Li, Interfacial optimization of g-C3N4-based Z-scheme heterojunction toward synergistic enhancement of solar-driven photocatalytic oxygen evolution, Appl. Catal., B 244 (2019) 240–249, https://doi.org/10.1016/j.apcatb.2018.11.056.

[91] W. Chen, J. Huang, Z.-C. He, X. Ji, Y.-F. Zhang, H.-L. Sun, K. Wang, Z.-W. Su, Accelerated photocatalytic degradation of tetracycline hydrochloride over CuAl2O4/g-C3N4 p-n heterojunctions under visible light irradiation, Sep. Purif. Technol. 277 (2021) 119461, https://doi.org/10.1016/j.seppur.2021.119461.

[92] Y. Cao, Y. Ren, J. Zhang, T. Xie, Y. Lin, Activation of H_2O_2 by photo-generated electrons for enhanced visible light driven methylene blue degradation with $ZnFe_2O_4$/BiVO4 heterojunction, Opt. Mater. 121 (2021) 111637, https://doi.org/10.1016/j.optmat.2021.111637.

[93] M. Hamandi, M. Meksi, H. Kochkar, Nanoscale advances of carbon-titanium dioxide nanomaterials in photocatalysis applications, Rev. Nanosci. Nanotechnol. 4 (2016) 1–27, https://doi.org/10.1166/rnn.2016.1065.

[94] M.A. Kanjwal, K.K.S. Lo, W.-W.-F. Leung, Graphene composite nanofibers as a high-performance photocatalyst for environmental remediation, Sep. Purif. Technol. 215 (2019) 602–611, https://doi.org/10.1016/j.seppur.2019.01.044.

[95] X. Wang, K. Maeda, A. Thomas, K. Takanabe, G. Xin, J.M. Carlsson, K. Domen, M. Antonietti, A metal-free polymeric photocatalyst for hydrogen production from water under visible light, Nat. Mater. 8 (2009) 76–80, https://doi.org/10.1038/nmat2317.

[96] Y. Cui, J. Huang, X. Fu, X. Wang, Metal-free photocatalytic degradation of 4-chlorophenol in water by mesoporous carbon nitride semiconductors, Catal. Sci. Technol. 2 (2012) 1396–1402, https://doi.org/10.1039/C2CY20036H.

[97] J. Ning, J. Zhang, R. Dai, Q. Wu, L. Zhang, W. Zhang, J. Yan, F. Zhang, Experiment and DFT study on the photocatalytic properties of La-doped Bi2WO6 nanoplatelike materials, Appl. Surf. Sci. 579 (2022) 152219, https://doi.org/10.1016/j.apsusc.2021.152219.

[98] K.M. Alam, C.E. Jensen, P. Kumar, R.W. Hooper, G.M. Bernard, A. Patidar, A. P. Manuel, N. Amer, A. Palmgren, D.N. Purschke, N. Chaulagain, J. Garcia, P. S. Kirwin, L.C.T. Shoute, K. Cui, S. Gusarov, A.E. Kobryn, V.K. Michaelis, F. A. Hegmann, K. Shankar, Photocatalytic mechanism control and study of carrier dynamics in CdS@C3N5 core-shell nanowires, ACS Appl. Mater. Interfaces 13 (2021) 47418–47439, https://doi.org/10.1021/acsami.1c08550.

[99] P. Saha, A. Sivaramakrishna, K.V.B. Rao, Bioremediation of reactive orange 16 by industrial effluent-adapted bacterial consortium VITPBC6: process optimization using response surface methodology (RSM), enzyme kinetics, pathway elucidation, and detoxification, Environ. Sci. Pollut. Res. 30 (2022) 35450–35477, https://doi.org/10.1007/s11356-022-24501-8.